STRUCTURAL AND ELECTRONIC PROPERTIES OF Cs-DOPED SiC:

A FIRST-PRINCIPLES INVESTIGATION

by

Tram Bui

A thesis

submitted in partial fulfillment

of the requirements for the degree of

Master of Science in Materials Science and Engineering

Boise State University

December 2012

© 2012

Tram Bui

ALL RIGHTS RESERVED

BOISE STATE UNIVERSITY GRADUATE COLLEGE

DEFENSE COMMITTEE AND FINAL READING APPROVALS

of the thesis submitted by

Tram Bui

Thesis Title: Structural and electronic properties of Cs-doped SiC: A first-principles investigation

Date of Final Oral Examination: 10 September 2012

The following individuals read and discussed the thesis submitted by student Tram Bui, and they evaluated her presentation and response to questions during the final oral examination. They found that the student passed the final oral examination.

Megan Frary, Ph.D.	Chair, Supervisory Committee
Pushpa Raghani, Ph.D.	Member, Supervisory Committee
Paul Millet, Ph.D.	Member, Supervisory Committee
Bill Knowlton, Ph.D.	Member, Supervisory Committee

The final reading approval of the thesis was granted by Megan Frary, Ph.D., Chair of the Supervisory Committee. The thesis was approved for the Graduate College by John R. Pelton, Ph.D., Dean of the Graduate College.

ACKNOWLEDGEMENTS

The Nuclear Regulatory Commission and Materials Science and Engineering Department at Boise State University funded this research under the supervision of Dr. Megan Frary. The investigation was conducted via computer simulation made available by the department and the Idaho National Laboratory. This thesis would not be done without the support of many people. I offer my most sincere gratitude to my advisor, Dr. Megan Frary, and co-advisor, Dr. Pushpa Raghani, for giving me guidance, intellectual support, and encouragement through the course of my thesis. And I also thank Dr. Paul Millet for being my third committee member and for his review of my work.

I offer many thanks to Dr. Izabela Szlurfarska and her team from the University of Wisconsin, Madison. This thesis would not have gone this far without their helps and the great support. I also thank Dr. Darryl Butt and Dr. John Youngsman at Boise State University for giving me valuable input and helping with the process of writing a thesis. I would like to thank all of the Materials Science and Engineering faculty members who have been a source of support and everyone in Dr. Frary's research group for all the material input.

Finally, I dedicate this work to my parents who have sacrificed many things in order for me to achieve my higher education, and thanks to my husband and all other family members for their love and emotional support.

ABSTRACT

The structural and electronic properties of pure and Cs-doped cubic zinc-blende silicon carbide (3C-SiC) were modeled by density functional theory in the plane-wave pseudo-potential formalism as implemented in the Quantum-ESPRESSO package. The equilibrium properties including lattice constant, bulk modulus, cohesive energy, and the indirect band gap energy were calculated for pure 3C-SiC. These values were compared with the experimental and theoretical values reported in the literature, and there was generally excellent agreement.

The influence of Cs on SiC in two structural configurations were modeled, including bulk SiC and a Σ3 grain boundary. The present investigation mainly focused on the neutral defects. To understand the stability of Cs in bulk SiC, the formation energies of isolated Cs defects and vacancy clusters were calculated. For the study of Cs in the grain boundary of SiC, only isolated Cs defects were modeled. Following the charge density and density of states calculations, the electronic structure of isolated Cs defects in bulk SiC was investigated. Relevant intrinsic SiC defect formation energies were also calculated. From the defect formation energies, it was predicted that the most probable stable state for neutral Cs in bulk SiC is for Cs to substitute for a Si atom with an associated C vacancy, Cs_{Si}-V_C. In the case of Cs migrating to a Σ3 grain boundary in SiC, it is predicted that the most probable state for neutral Cs is for Cs to sit on a Si site at the boundary without an associated defect.

TABLE OF CONTENTS

ACKNOWLEDGEMENTS iv

ABSTRACT v

LIST OF TABLES viii

LIST OF FIGURES ix

CHAPTER 1: INTRODUCTION 1

1.1: Motivation 1

1.2: Objectives 2

CHAPTER 2: BACKGROUND 3

2.1: Density Functional Theory 3

2.1.1: The Impacts of DFT on Materials Research 3

2.1.2: Physical Aspects of DFT 5

2.1.3: Exchange-Correlation Functional Approximation Methods 9

2.1.4: Reciprocal Space (Brillouin Zone) and *k*-Points 10

2.1.5: Pseudo-Potential 12

2.2: Structure and Performances of TRISO Fuel 14

2.3: Silicon Carbide 17

2.4: Diffusion of Fission Products in TRISO Fuels 19

CHAPTER 3: COMPUTATIONAL DETAILS 24

3.1: Theoretical Approach 24

3.2: Defect Formation Energy 27
3.3: Testing Convergence 30
3.3.1: Lattice Parameter and *k*-Point Convergence 30
3.3.2: Kinetic Energy Cutoff for Plane Wave Function 33
CHAPTER 4: RESULTS AND DISCUSSION 36
4.1: Bulk 3C-SiC 36
4.2: Cs in Bulk 3C-SiC 40
4.2.1: Charge Distribution 42
4.2.2: Density of States 46
4.2.3: Defect Formation Energy 50
4.3: Cs at Σ3-Grain Boundary SiC 55
4.3.1: Intrinsic SiC Defect Energies 56
4.3.2: Cs Point Defects in the Grain Boundary of SiC 61
CHAPTER 5: SUMMARY AND FUTURE WORK 64
REFERENCES 66

LIST OF TABLES

Table 1 Summary of Cs and Ag diffusion coefficients in SiC 21

Table 2 The results of the total energies and lattice constant computed with M×M×M *k* points. 32

Table 3 Primary parameters for calculations in bulk 3C-SiC with 1×1×1 and 2×2×2 super cells 37

Table 4 Equilibrium lattice constant, Bulk modulus, and cohesive energy with respect to the calculation method and *k*-points 38

Table 5 Band gap energy of 3C-SiC based on density functional theory calculations in comparison with the experimental data 39

Table 6 Theoretical lattice constants of 3C-SiCwith and without Cs point defects 41

Table 7 Data of electrons gained to the s, p and d orbitals of Cs atom in each defect type. 46

Table 8 The binding energy of Si, C and SiC compound 51

Table 9 Chemical potential of Si and C atoms in Si-rich and C-rich conditions compare with data reported from Shrader *et al.* 51

Table 10 Intrinsic defect formation energies (eV) for Si and C vacancy in 3C-SiC 52

Table 11 Defect formation energies of neutral Cs defects in bulk 3C-SiC under the two boundary conditions of the chemical potential: Si-rich and C-rich. .. 54

Table 12 Results of formation energies for intrinsic defects in the bulk and at the grain boundary of SiC 60

Table 13 Results for neutral Cs substitution defect formation energies in GB SiC. 62

LIST OF FIGURES

Figure 1 Difference perspective of the density functional theory versus the reality for the many-body system. 6

Figure 2 A typical computational procedure of calculating the total ground state energy and related quantities. 9

Figure 3 The all electron (AE) and pseudo (PS) wave functions for the valence energy states of cesium atom. The matching occurs beyond the cutoff radius. 13

Figure 4 Structure of the coated TRISO particle 15

Figure 5 Typical fission products release profile during linear temperature ramp up [1]. 17

Figure 6 Crystal Structure of 3C-SiC 18

Figure 7 The XZ cross sectional structure of the bi-crystal grain boundary model. The red line represents the grain boundary plane separating the grain 1 (G1) and grain 2 (G2). Only one layer of atoms is shown here while the others are into the page. 26

Figure 8 Total energy, of zinc-blend 3C-SiC structure, as a function of lattice parameter. The solid curve corresponds to the fit of DFT data. The plot was obtained using Mathematica 8 program. 31

Figure 9 Total energy of SiC (as described in Table 2) plotted as a function of M for calculations using M×M×M *k*-points. 33

Figure 10 Lattice constant, as described in Table 2, plotted as a function of M for calculations using M×M×M *k* points. 33

Figure 11 The total energy of the bulk SiC calculated as a function of kinetic cutoff energy. 34

Figure 12 The total energy of grain boundary SiC plotted as a function of *k* points. 35

Figure 13 Band structure of 3C-SiC calculated at the equilibrium volume. The Fermi level is taken as the zero of energy. 39

Figure 14 Crystal structure of Cs interstitial at the octahedral site (a), Cs substitution C site (b), and Cs substitution Si site (c)... 42

Figure 15 Charge density of bulk 3C-SiC along the (110) plane. 43

Figure 16 The charge density along the (110) plane of the Cs point defects in 3C-SiC system: Cs_C (a), Cs_{Si} (b), and Cs_i (c)... 44

Figure 17 Density of states as a function of energy for bulk 3C-SiC. The band gap energy is indicated as E-gap and the Fermi level is at zero. 47

Figure 18 Total density of states of 3C-SiC with and without Cs defects along with the partial density of state of Cs's 5d orbital, where (a) is Cs_C, (b) is Cs_{Si}, and (c) is Cs_i. 49

Figure 19 Crystal structure of single C vacancies in GB SiC includes: the complete GB SiC structure with three original C atoms (top left), C vacancy at GB plane (top right), C vacancy at G1 (above the GB plane) (bottom left), and C vacancy at G2 (below the GB plane) (bottom right). 58

Figure 20 Crystal structure of single Si vacancies in GB SiC includes: the complete structure of GB SiC with three original Si atoms (top left), Si vacancy at GB plane (top right), Si vacancy at G1 (bottom left), and Si vacancy at G2 (bottom right). 59

CHAPTER 1: INTRODUCTION

1.1: Motivation

The fractional release of radioactive fission products through the SiC boundary layer in the Tristructural-Isotropic (TRISO) fuel particles has become a critical issue during the operation process of the very high temperature gas cooled reactors [1]. Each TRISO particle has a nucleus, which usually consists of uranium dioxide, uranium carbon oxide (UCO), or uranium di-carbide, which is surrounded by layers of porous carbon, pyro-carbon (PyC), and silicon carbide [1]. The SiC layer is a main constituent in the TRISO particle due to its high chemical and thermal stability, and excellent resistance to corrosion and neutron radiation damage [2]. To achieve good fuel performance, it is important to choose a high quality SiC material. The SiC layer provides structural support and serves as the main barrier to retain metallic fission products (e.g., Ag and Cs whose half-lives are 253 days and 30 years (^{137}Cs), respectively) released by the fuel kernel during reactor operation [3]. However, SiC has been found less effective in containing Cs and Ag ions than was expected [1]. Studies have shown a large amount of Cs and Ag released into the reactor under the operation of TRISO fuel [1]. Having radioactive fission products in the coolant can be a great potential threat to the environment and society [4]. In addition, Cs is an explosive and radioactive material, which makes it an external hazard (i.e., a hazard even without being taken into the body) [5]. In order to reduce the rate and understand the causes of Cs release from TRISO fuel, the theoretical study of the thermodynamics and kinetics of Cs in SiC will provide more solid evidence

on what effects Cs has on the material structure and properties of SiC and what possible diffusion mechanisms of Cs could be in SiC. In addition, understanding the thermodynamics and kinetics of Cs in SiC allows the process parameters of producing SiC such as temperature, alloy composition, and layer thickness to be adjusted to optimum values under certain service conditions, which will improve the performance of SiC in TRISO fuel [6].

1.2: Objectives

The objective of the thesis was to develop a simulation model and carry out a variety of calculations such as the total ground state energy, the density of states, the band structure, and the valence electron density. The model allows an investigation of the material properties in bulk 3C-SiC and what changes Cs brings to SiC when Cs is in different defects configurations such as interstitial, substitution, and at grain boundary sites. In addition, because the intrinsic defects play an important role in mediating the diffusion of impurities, silicon and carbon vacancies were also studied in the bulk and in the grain boundary of SiC. Due to the requirement of long computational time, only neutral Cs defects were studied in this project in order to determine the most stable impurity that requires the lowest defect formation energy. In this project, computational integration-based DFT was used to predict the influences of Cs in bulk and along or across a Σ3-grain boundary of SiC.

CHAPTER 2: BACKGROUND

2.1: Density Functional Theory

Over the past decade, due to the rapid development of modern materials and devices, the study and characterization of materials at the atomistic level, from synthesis to assembly, have been great challenges. As the laws of quantum mechanics govern the interaction between atoms and electrons [7], a quantum mechanical analysis technique is required to solve a basic quantum mechanical equation for complex many-atom, many-electron systems [7]. In 1964, Walter Kohn and his co-workers developed density functional theory (DFT), which allowed an analytical solution to the Schrodinger equation for many-atom, many-electron systems [7]. DFT has opened a new door for research in physics, materials science, chemistry, nanotechnology, and even earth sciences and molecular biology [7].

2.1.1: The Impacts of DFT on Materials Research

Density functional theory is one of the most common methods for ground state electronic structure calculations in quantum chemistry and solid state physics [8]. Density functional theory allows for solution of the Schrödinger equation for many-atom or many-electron systems as a function of charge density, rather than solving the wave function. In many-electron (many-body) systems, the self-interactions, also known as exchange-correlation relations, cause electrons to be indistinguishable, leading to the fact that energy and forces are impossible to be solved analytically. DFT provides a balance

between computational cost and accuracy that allows quantitative data to be computed for any material model (up to thousands of atoms) [9]. Therefore, the computational work based on DFT is well suited to a variety of material science applications such as surface science and catalysis, structural metals and earth sciences, semiconductors, nanotechnology, and biomaterials [7].

The applications of DFT, through various computational techniques, to accelerate the design processes and enhance material properties are used widely in numerous structural materials such as steels, aluminum cast alloys, and titanium alloys [7]. In 2004, Csanyi *et al*. used a molecular dynamics approach in combination with classical force-field embedded quantum-mechanical models to study crack propagation in silicon [10]. In this study, they used a model containing about 200,000 atoms, which shows that DFT calculations can be done on a large material model with the support of a high-speed computer system [10]. DFT is also being used in surface science to understand the atomic-scale mechanisms of chemical reactions on surfaces as well as to describe the rates of heterogeneous catalysts reactions [7].

In other fields such as biomaterials, DFT plays an important role in studying the complex process of biological materials [7]. Besides that, DFT has been used widely in the studies of semiconductors, where electronic properties such as band gaps and defect states can be performed for unary and binary systems [7]. In addition, DFT has proven to be a powerful method for studying defects in solids [11]. DFT provides a standard tool to investigate the defects concentration in solids in thermal equilibrium, the defects interactions, and their vibration modes, which are all associated with the ground state of the defect [11]. Overall, DFT yields a comprehensive description of materials from

crystal structure to phase stability, from mechanical properties to electrical properties, and from dielectric to magnetic properties [7]. Hence, DFT has become robust and has enabled many tasks to be performed automatically. With the increasing speed of computers nowadays, DFT opens a way toward high-throughput computation for various materials research fields.

2.1.2: Physical Aspects of DFT

An atom consists of a positive nucleus and electrons moving around it. The motion of electrons and their behaviors determine the chemical properties of an atom such as the interaction with other atoms, the formation of molecules, electrical conductivity, and others. In a quantum mechanics model, the Schrödinger equation determines the probability of finding an electron as a function of space and time. However, it is impossible to solve for more than a few electrons because each electron not only interacts with the nucleus, but also with other electrons. As more electrons are added to a material, solving the problem becomes more difficult for even a computer to handle. In 1964, Kohn and Hohenberg developed DFT [12]. In DFT, the interactions of the electrons and the nucleus can be obtained by a model called electron density. Electron density is the probability of finding an electron in space. Basically, electron density depends only on three spatial coordinates, while many-body wave functions depend on all spatial coordinates of all electrons [13]. Therefore, electron density provides a simple method to solve the Schrödinger equation and it is a desirable computational property of DFT. An illiustration of how electrons are treated in the DFT perspective compared to their complex interactions in many-body system is shown in Figure 1. In the DFT

perspective, all electron-electron interactions are treated through the electron density, which holds atomic ions together inside a molecule or a solid [13].

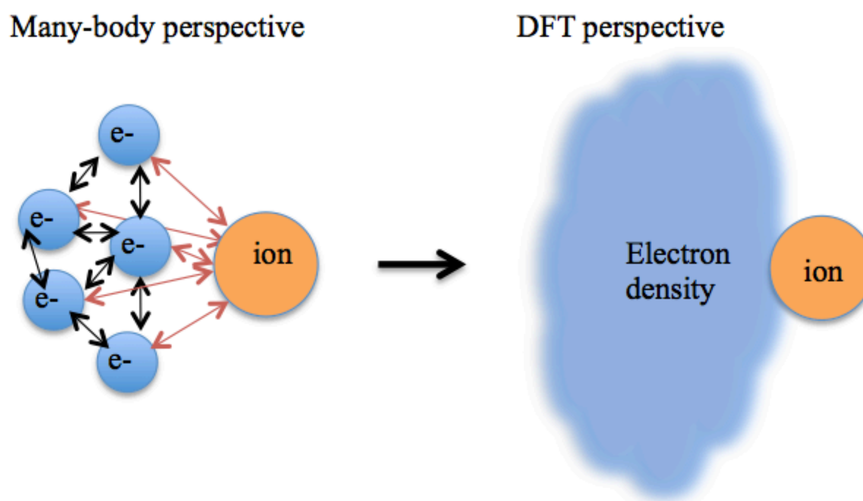

Figure 1 Difference perspective of the density functional theory versus the reality for the many-body system.

The key justification of DFT rests on two fundamental mathematical theorems proved by Hohenberg and Kohn [12]. The first theorem states that the total ground state energy, E_0, from the Schrödinger equation is a unique functional of the ground state charge density, $n_0(r)$, which can be described as the following function:

$$E_0 = E\,[n_o(r)] \qquad \textbf{[2.1]}$$

The second theorem states that the ground state energy can be found by the minimization of the overall functional above with respect to the electron density, which corresponds to the full solution of the Hamiltonian equation:

$$E_0 = \frac{\partial\, E[!\ (r)]}{\partial\, n(r)}\Big|_{n=n_0(r)} = \frac{\langle \Psi_0 | H | \Psi_0 \rangle}{\langle \Psi_0 | \Psi_0 \rangle} \qquad \textbf{[2.2]}$$

where E[n(r)] is the energy functional of charge density, n(r), H is the Hamiltonian operator, and Ψ_o is the probability of finding the electron at its ground state energy. Notice that Ψ_o is a function of the coordinates of all electrons, while n(r) is a function of three spatial coordinates only. The energy functional, E [n(r)], can be written in the form of single-electron wave functions, ψ_i(r), which define the electron density n(r):

$$n(r) = 2 \sum_i \psi_i^* (r) \psi_i(r) \qquad \textbf{[2.3]}$$

$$E[\{\psi_i\}] = E_{know}[\{\psi_i\}] + E_{xc}[\{\psi_i\}] \qquad \textbf{[2.4]}$$

where $E_{know}[\{\psi_i\}]$ includes four analytical contributions that can be analytically calculated:

$$E_{know}[\{\psi_i\}] = -\frac{h^2}{m}\sum_i \int \psi_i^* \nabla^2 \psi_i d^3(r)$$

$$+ \int V(r)n(r)d^3(r) + \frac{e^2}{2}\int \int \frac{n(r)n(r')}{|r-r'|} d^3(r)\, d^3(r') + E_{ion}$$

The terms on the right-hand side represent the electron kinetic energies, the Coulomb interaction between the electrons and the nuclei, the Coulomb interactions of electrons pairs, and Coulomb interactions between pairs of nuclei, respectively. In Eq. (2.4), $E_{xc}[\{\psi_i\}]$ is an exchange correlation energy, which is defined to include the entire quantum mechanical effects that are not included in $E_{know}[\{\psi_i\}]$. Therefore, $E_{xc}[\{\psi_i\}]$ is not exactly determined and needs to be meaningfully approximated. In order to find the right electron density that can minimize the energy functional of Eq. (2.4), the set of one-particle equations, called Kohn-Sham equations, were developed with an additional correction to the effective potential:

$$\left\{-\frac{1}{2}\nabla_i^2 + v_{eff}(r)\right\}\psi_i(r) = \varepsilon_i\psi_i(r) \qquad \textbf{[2.5]}$$

$$v_{eff}(r) = v(r) + \int \frac{n(r')}{|r-r'|} d(r') + v_{xc}(r) \qquad \textbf{[2.6]}$$

$$n(r') = \sum_{i=1}^{N} |\psi_i(r')|^2 \qquad \textbf{[2.7]}$$

where in Eq. (2.5), $-\frac{1}{2}\nabla_i^2$ represents the kinetic energy of electron, $v_{eff}(r)$ is the effective potential (defined in Eq. (2.6)), and ε_i is the ground state Eigen value. On the right side of Eq. (2.6), the term v(r) is the potential defining the interaction between electrons and the collection of the nuclei, called the atomic potential. The second term is the Hartree potential and the last term, $v_{xc}(r)$, can be defined as a functional derivative of the exchange-correlation energy [9, 12, 14].

$$v_{xc}(r) = \frac{\partial E_{xc}(r)}{\partial n(r)} \qquad \textbf{[2.8]}$$

All the Kohn-Sham equations must be solved self-consistently. A schematic flow chart in Figure 2 shows the typical computational procedure for any DFT-based calculation. The procedure requires an input, which is a geometrical arrangement of atoms determining the overall atomic potential v(r), and the atomic number Z. It also requires an initial guess for the electron charge density, from which the exchange-correlation potential and the Hartree potential can be calculated [15]. The self-consistent loop solves the Kohn-Sham equations using numerical schemes. A typical self-consistency is achieved when the generated charge density is smaller than the chosen values [15].

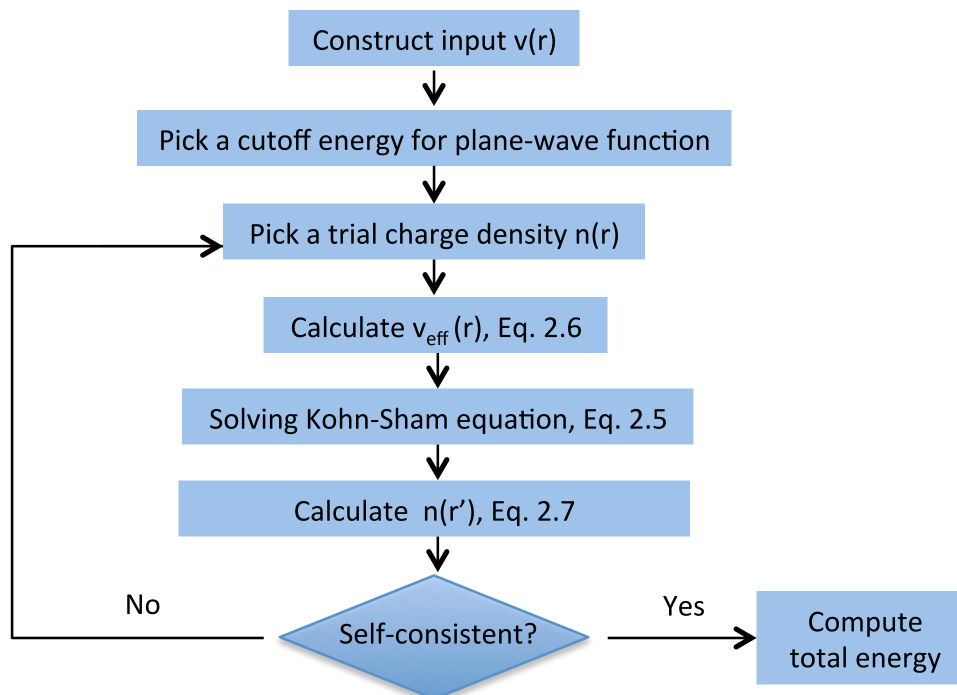

Figure 2 A typical computational procedure of calculating the total ground state energy and related quantities.

2.1.3: Exchange-Correlation Functional Approximation Methods

DFT has two practical limitations. One is the need to approximate the exchange-correlation functional. The other is that properties calculated by DFT need to be formulated as a function of electron density. In addition, various numerical approximations will also affect the results [13]. The Kohn-Sham equations reformulate the many-body Schrödinger equation as a set of one-electron equations, where all of the many-body interactions are contained in the exchange-correlation functional, $E_{xc}[\{\psi_i\}]$. As mentioned above, the exact form of this functional is unknown and an approximation must be used. Several approximations were developed by Perdew [12]. The most common framework of DFT is the local density approximation (LDA), where the exchange-correlation potential at each position is set to be the known exchange-correlation of the infinite homogeneous electron gas with the same electron density.

$$E_{xc}(r) = E_{xc}^{electron\ gas}[n(r)] = \int \varepsilon_{xc}[n(r)]\, n(r) d^3r \qquad \textbf{[2.9]}$$

where $\varepsilon_{xc}[n(r)]$ represents the exchange-correlation energy per electron. The local density functional approximation uses only the local electron density to approximate the exchange-correlation, which is not the true exchange-correlation functional [12]. Therefore, the results of the Kohn-Sham equations do not exactly solve the true Schrödinger equation. Another choice of exchange-correlation is the generalized gradient approximation, which uses the local electron density and the local gradient in the electron density. Therefore, the generalized gradient approximation should be more accurate than the local density approximation functional. However, this is not always true [9]. In GGA, there are different ways to include the information from the gradient of the electron density. The most two common functions are the Perdew-Wang functional (PW91) and the Perdew-Burke-Ernzerhof functional (PBE) [9]. Many more GGA functionals have been developed and used such as the Meta-GGA functional (an addition variable of the kinetic energy density is used) or the Hyper-GGA functional [9]. Each function gives a different result for a particular atomic configuration, even though the difference can be very small. Therefore, it is necessary to specify what functional was used in a calculation rather than just "a DFT calculation" [7].

2.1.4: Reciprocal Space (Brillouin Zone) and *k*-Points

In materials research, DFT is used for calculations in a system with periodic atoms in space. The cell, containing these atoms, which is repeated periodically, is called the super cell. The super cell is defined by the lattice vectors a_1, a_2, and a_3. In order to solve the Schrödinger equation for a periodic system, the solution must satisfy Bloch's theorem, in which the solution can be expressed as:

$$\phi_k(r) = e^{ikr}u_k(r)$$

where k is a wave vector confined to the first Brilliouin zone, r is a position vector that defined a point in space, and $u_k(r)$=$u_k(r + n_1a_1 + n_2a_2 + n_3a_3)$ for any integers n_1, n_2, and n_3 is a periodic function that is periodic in space with the same periodicity as the super cell. Bloch's theorem indicates that the Schrödinger equation can be solved independently for any value of k. Many parts of the mathematical problems posed by DFT are easier to solve in terms of k rather than r [12]. Because the expansion of e^{ikr} expresses the original plane waves, the calculations based on this equation are defined as plane-wave calculations. Plane waves allow for taking advantage of the fast Fourier transformation (FFT), hence it is the most numerically convenient basis set that can be used in DFT. The space with respect to vector r is called real space, and to vector k is called reciprocal space (or k space) [12].

In k space, a primitive cell is the minimum volume containing all of the information of the material. The concept of the primitive cell in k space follows the Wigner-Seitz cell, in which the reciprocal lattice vectors can be defined as easily as it can be in real space. The cell in k space is often called the Brillouin zone, which contains several k-points with special significance of symmetry. These points are given individual names. The most important point is called the gamma point (Γ point), which is the center of the reciprocal space (i.e., k=0 at the Γ point) [12].

DFT calculations require significant computational effort; therefore, integration of the mathematical equations cannot take place over the entire k space. Monkhorst and Pack [12] developed a solution, wherein a grid of points in k space is considered. For a super cell that has the same length in all directions (e.g., a cubic lattice), the same number

of *k*-points is used in each direction. The calculation is then labeled as using M×M×M *k*-points. In general, it is expected that using M will give more accurate results than N, if M>N. However, in practice, to decide how many *k*-points will be used depends on the material system. If the calculated total energy is almost independent of the number of *k*-points, then one can expect that all calculations in *k* space are well-converged, and thus there is no need to use a large set of *k*-points [12]. More details on the use of *k*-point will be discussed in Section 3.2.2.

2.1.5: Pseudo-Potential

The atomic potential v(r) in Eq. (2.6) describes the electrostatic interaction of the nucleus with the surrounding electrons. While each atom contains core electrons and valence electrons, only the valence electrons contribute to the chemical bonding of that atom. In order to reduce the cost of the computational calculations, a method of handling only valence electrons is developed, which is called the pseudo-potential approach [16]. In this method, the “fixed” core electrons are eliminated. Inside the core region, the valence electron wave function, due to the orthogonality to the core electron wave function, is described by a smooth node-less wave function while it is matched with the true wave function outside the core region [17]. A calculation without the frozen core is called an all-electron calculation. An illustration of matching wave functions in a pseudo-potential approach is shown in Figure 3. The arrows indicate the cutoff radius of the wave functions, where the left of the arrow is fixed as the “frozen core” and the wave function is replaced by a smooth node-less function (e.g., green replaces red for the 6s state). To the right of the arrow (outside the core), the pseudo-wave function matches the all-electron wave function. The same behavior is shown for the 5s state, where the cutoff

radius is set at a different value. This indicates that each valence state is set with a specific cutoff radius in the pseudo-potential approach. In this approach, the wave function that is smooth both inside and outside the core is the so-called pseudo-wave function.

The pseudo-potential approach makes a big impact on improving the performance of DFT because the smooth functions can be expanded easily in plane wave calculations [12]. Moreover, the pseudo-potential helps reduce the computational cost due to the elimination of the interactions from the core electrons. Some useful reviews on the pseudo-potential approach and full-electrons augmented wave methods can be found in Refs. [18-19].

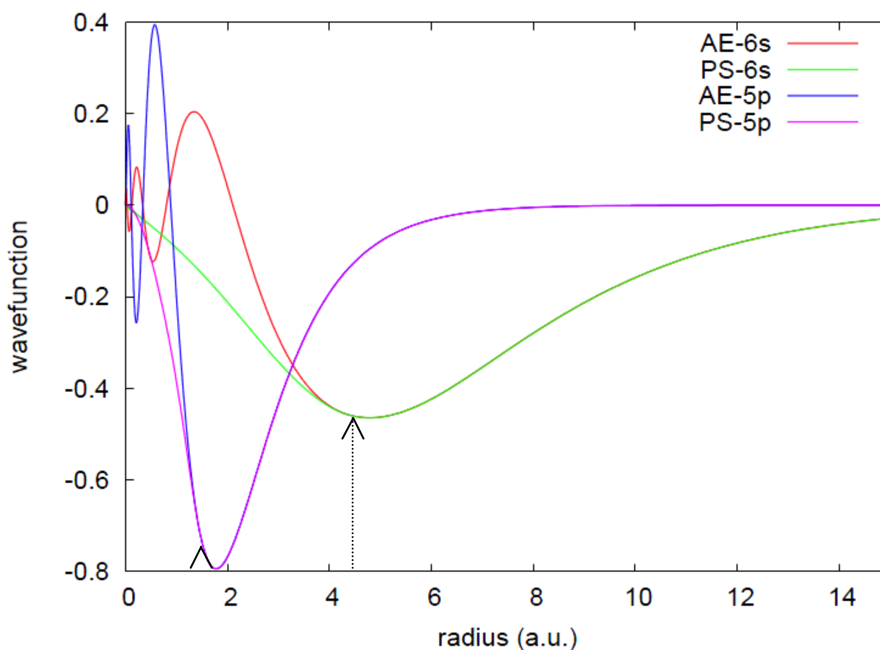

Figure 3 The all electron (AE) and pseudo (PS) wave functions for the valence energy states of cesium atom. The matching occurs beyond the cutoff radius.

2.2: Structure and Performances of TRISO Fuel

TRISO fuel is typically made in the form of rods or spheres (also known as pebbles) consisting of a graphite matrix and coated with a graphite layer [1]. Figure 4 shows a fuel sphere is made up of a 60 mm diameter sphere of graphite matrix and with a 5 mm thick-coated graphite layer. Each sphere contains thousands of TRISO coated particles and each coated particle usually contains a kernel of UO_2 (fuel produced by Germany), UCO, or UC_2 (fuel produced by the US) [20]. Figure 4 also shows a buffer layer of carbon and three other layers of carbide that coat the particle: an inner PyC, SiC, and then an outer PyC layer. Each particular layer provides certain structural support to the TRISO particle to sustain irradiation during the fission process. Among the coatings, the SiC layer plays an important role in capturing any fission products emitted by the nucleus. Therefore, the quality of SiC is vital to the performance of the TRISO coated particle [21]. The material properties of SiC will be discussed in more detailed in Section 2.3.

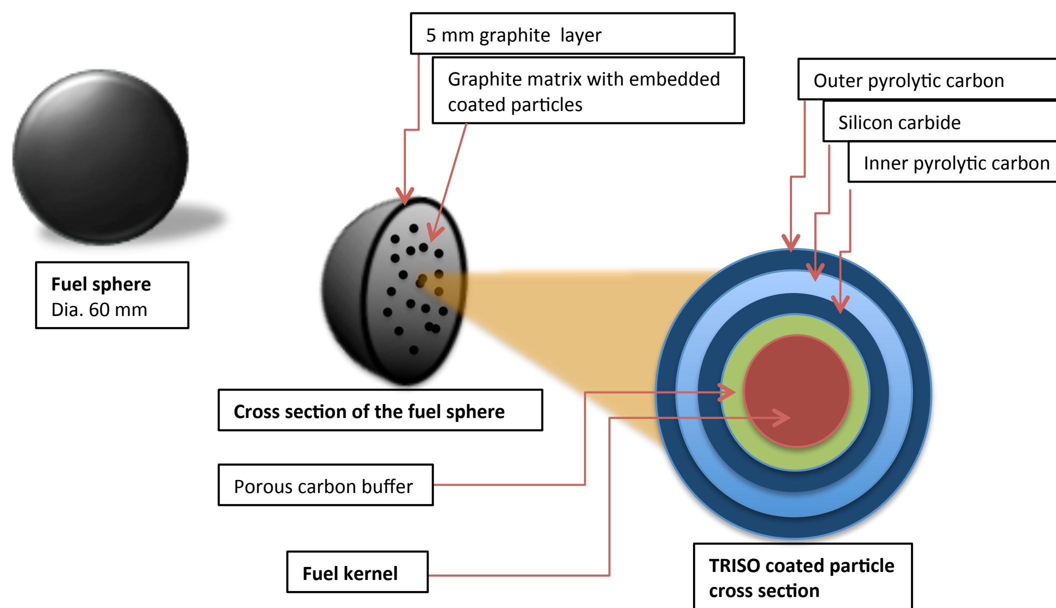

Figure 4 Structure of the coated TRISO particle

TRISO fuel is widely used in high temperature gas-cooled reactors (HTGRs) due to the stable structure of the fuel particles under the extreme operating environment [22]. Using TRISO fuel for HTGRs in nuclear plants will reduce the use of fossil fuel such as oil and natural gases, which will help improve overall energy security in the U.S. by reducing dependence on foreign fuels and reducing CO_2 emissions [6]. However, many studies have shown that materials degradation in a nuclear power plant has become a critical issue due to the harsh environment (i.e., high temperature gradient, corrosion, neutron radiation) where materials have to endure during the lifetime of a nuclear power system. Currently, the lifetime is expected to be from 40 to 60 years [23]. During service, the materials experience a corrosive environment, steep temperature gradients, and high-energy particles released during fission. The fuel that provides power to the reactor usually has a much shorter lifetime than the structural components, but is also subjected

to the same harsh environment [6]. Therefore, it is a challenge to study the material failures of many fuels, including TRISO fuel.

As discussed in Section 1.1, the SiC layer plays an important role in determining the performance of TRISO fuel; there have been many studies focused on the failure of the SiC layer [1, 22, 24]. It has been proven that the failure of SiC occurred under extreme high temperature conditions and primarily depended on the thermal properties of the TRISO coatings [1, 24]. In addition, the studies showed that the fission product retention depended primarily on the properties of the TRISO coatings [1]. Therefore, failure of the SiC layer at high temperature will increase the diffusion rate of fission products [1]. Figure 5 shows that as the particles are heated up to very high temperatures, the release rate of fission products such as Ag, Cs and Kr is much higher [1]. At an elevated temperature (>1373K), the release rate of Ag, Cs, and Kr from the fuel increased rapidly [1]. Among the fission products, ^{137}Cs is one of the most hazardous and dangerous radioisotopes [25]. To reduce the release of Cs from the fuel particle, it is critical to have good quality coating materials, especially SiC [1]. By understanding the interaction of fission products within the SiC layer, a better material that exhibits low failure rates can be designed.

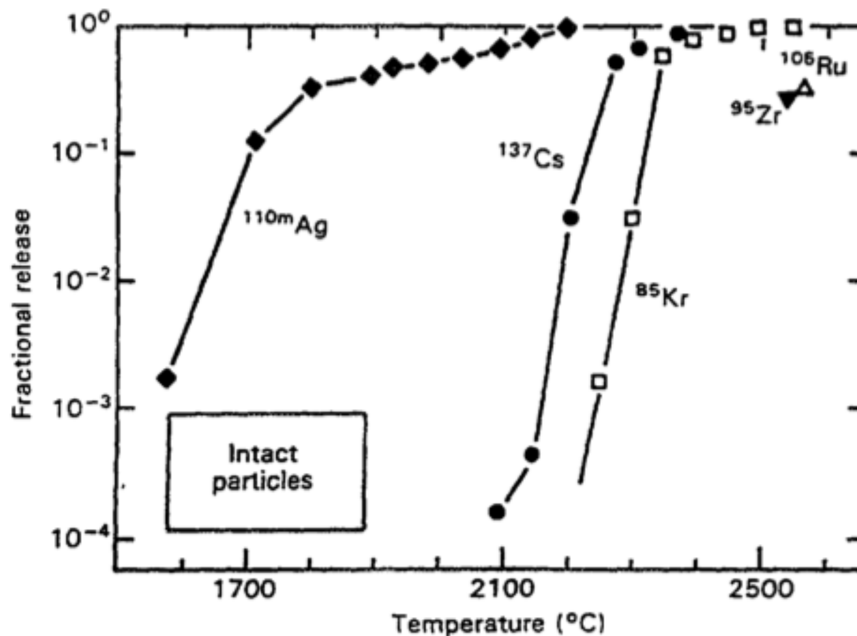

Figure 5 Typical fission products release profile during linear temperature ramp up [1].

2.3: Silicon Carbide

SiC has more than 250 polytypes resulting from the wide variety of stacking sequences of Si-C atomic planes. The most common polytypes are 3C, 4H, 6H, and 15R, where C, H, and R represent cubic, hexagonal, and rhombohedral crystals, respectively. The 3C-SiC crystal is known as β-SiC, which is also the only Si-C stacking sequence that shows cubic symmetry. All other polytypes that show non-cubic symmetry are specified as α-SiC [26]. The stoichiometric cubic SiC (β-SiC) is found to be more stable than the hexagonal structure at temperatures below 2373 K (~2100°C). The experimental lattice parameter and density of β-SiC are 4.358 Å and 3.21 g/cm^3, respectively [2, 26].

The β-SiC has a zinc-blende crystal structure, where C atoms are located at the tetrahedral sites. With a close-packed structure, SiC has a higher specific heat as well as melting temperature compared to other refractory carbides or nitrides [2]. The atomic

structure of a 1×1×1 SiC unit cell is shown in Figure 6, which shows the face-centered arrangement of silicon atoms with carbon atoms in half the tetrahedral sites.

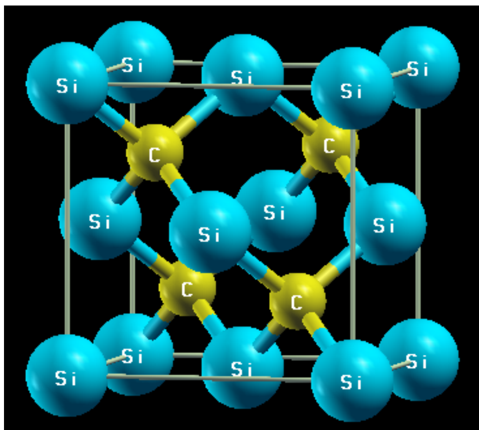

Figure 6 Crystal Structure of 3C-SiC

The Si-C bonds in 3C-SiC are not only covalent but also have a slight ionic character [2, 26]. Due to the difference of electro-negativity between Si and C, 1.9 and 2.55 respectively [27], it is expected that some electrons will be transferred from silicon to carbon. In addition, 3C-SiC has wide electronic band gap, ~2.4 eV, high thermal conductivity (~350 W/m K), and thermal expansion coefficient (~ $4.4 * 10^{-6}$/K) [2, 26]. Therefore, SiC is used as a structural material for a variety of high-temperature applications, high power devices, and in the nuclear industry [28]. Along with high chemical and thermal stability, and good resistance to neutron radiation damage, SiC became a great choice of material for TRISO fuel in gas-cooled nuclear fission and fusion reactors [29]. However, under the extreme radioactive environment, the SiC layer is found to be less effective in retaining the fission products such as Cs and Ag in TRISO fuel [3, 30]. Several studies performed phase change analysis on SiC at high temperatures [1]. The studies showed that the transition of β-SiC to α-SiC occurred in the temperature

range from 1973 K to 2473 K [1]. Fission product release rates were found to be consistent with the consequence of the failure mechanism initiated by a β-SiC phase transition to α-SiC [1]. The phase transition at high temperatures essentially increases the percentage of porosity, disorder, and complete thermal decomposition of SiC material in TRISO particles, which could potentially be the cause of material failures. As a result, fission products could be released due to these failures [1].

The SiC layer used in TRISO-coated fuel particles is normally produced at 1500^oC- 1650^oC via fluidized bed chemical vapor deposition of methyl-trichloro-silane (CH_3SiCl_3) using hydrogen as the fluidizing gas [31]. In order to retain the fission products, SiC must have a density closed to ~3.21 g/cm^3 [32]. It is difficult to reproduce SiC with the same material properties (i.e., density, hardness, tensile strength) because under different laboratories and process parameters such as deposition rates, temperatures, and fluidizing bed condition, SiC will have different properties [32].

2.4: Diffusion of Fission Products in TRISO Fuels

Several works have studied the fundamental mechanism of Cs, Ag, and Pd transport through the SiC layer [1, 32-33]. Within these studies, three methods were used to determine the effective diffusion coefficients of metallic fission products. Amian and Stover [32] studied the fractional release of Ag and Cs from irradiated silicon-carbide-layered coated particles using an integrated release method. The particles were annealed between 1273 K and 1773 K for several time periods. Their procedure begins with measuring the content of fission products of each particle (^{137}Cs and ^{110}Ag) using anti-Compton gamma spectrometry with a central Ge(Li) detector. The particles are then annealed and the released fission products were collected on the water-cooled copper

plates [32]. The effective diffusion coefficients were derived by fitting the diffusion model to the overall integrated release data obtained from a batch of TRISO fuel particles. The effective diffusion coefficients follow an Arrhenius relation [3, 32]:

$$D^{eff} = D_o(\, m^2 s^{-1}) * Exp\left(\frac{-Q\ (kJ.mol^{-1})}{k_b T}\right) \qquad \textbf{[2.1]}$$

where k_b is the Boltzmann constant, D_o is the constant pre-factor, and Q is the activation energy of the diffusion mechanism. In their investigation, the effective diffusion coefficients are evaluated by simulating Fickian diffusion through the TRISO coating and by adjusting the diffusion coefficients to match the observed fission product release [32].

The second method measured the effective diffusion coefficient via ion-implanted cubic 3C-SiC samples. Only SiC and the fission product were involved using this method. Therefore, the experiments performed on TRISO-coated particles were more straightforward and easier to interpret than the integral release (IR) method [33-34]. The third method used a diffusion couple, where the fission products are in direct contact with SiC and their diffusion into SiC can be studied under different annealing conditions [34].

Table 1 shows the experimentally determined diffusion coefficients and the activation energies (Q) for Ag and Cs diffusion in SiC from various references, including the temperature range and the method by which the works were carried out. For Cs diffusion, the data show a significant change in diffusion mechanism at temperatures around 1673 K. At temperatures below 1673 K, the activation energy ranges from 1.3 to 2.5 eV; above 1673K, the activation energy is greater than 5 eV [1, 32]. The rapid change in activation energies indicates a change in diffusion mechanism. It suggests at low temperature, grain boundary diffusion is a dominant mechanism in SiC, while bulk

diffusion dominates at high temperature [3]. For Ag, there is no evidence of a sudden change in activation energy, and the certainty about diffusion mechanisms was unclear. The variation in diffusion coefficients between the similar integral release measurements, which were done with different SiC microstructures, suggests that the SiC microstructure plays an important role in Ag diffusion [30]. In general, Table 1 also shows the variation in the diffusion coefficients and the activation energies values; this indicates the uncertainty among the experiments. Therefore, theoretical studies must be done to provide more solid results.

Table 1 Summary of Cs and Ag diffusion coefficients in SiC

Reference	Fission product	Do (m^2/s)	Q (eV/atom)	Temperature (K)	Measurement method
[1]	Cs	5.50×10^{-14}	1.30	1073-1673	IR
[32]	Cs	3.50×10^{-9}	2.45	1273-1773	IR
[35]	Cs	1.17×10^{-11}	1.82	1273-1873	-
[1]	Cs	1.60×10^{-2}	5.33	1673-1973	IR
[36]	Cs	2.50×10^{-2}	5.21	1873-1973	IR
[1]	Ag	4.50×10^{-9}	2.26	1273-1773	IR
[37]	Ag	6.76×10^{-9}	2.21	1073-1773	IR
[38]	Ag	5.00×10^{-10}	1.89	1273-1773	IR
[38]	Ag	3.5×10^{-10}	2.21	1473-2573	IR
[33]	Ag	4.30×10^{-12}	2.50	1473-1673	Ion-implant
[34]	Ag	$D<5.0\times10^{-21}$	-	1773	Ion-implant

To obtain a better understanding of diffusion mechanisms of Ag and/or Cs in SiC, over the past few years, ab initio modeling of Ag and Cs defects and their mobility in bulk and grain boundary SiC were studied by Shrader *et al.* [3, 30] and Khalil *et al.* [39].

Their studies involved the diffusion of Ag in both the bulk and the grain boundaries of SiC. They also investigated the diffusion of Cs in bulk 3C-SiC.

For Ag diffusion in bulk SiC, defect formation energies were calculated for intrinsic defects such as Si vacancies (V_{Si}), C vacancies (V_C), and Si substitution of C (Si_C). The structure and stability of charged Ag and Ag vacancy clusters in SiC were then investigated. The most stable Ag defect in SiC was found to be a silver atom substituting on the silicon sub-lattice and bound to a C vacancy (Ag_{Si}-V_C) [30]. The Ag interstitial impurity was found to have the lowest activation energy of ~7.9 eV [30]. The calculated activation energies were high compared to the values from the experimental data and this would cause Ag to diffuse slowly in the bulk SiC. As a result, Ag transport in SiC can be through an alternative mechanism such as grain boundary diffusion [30].

In order to prove that the hypothesis of Ag release from TRISO fuel might occur through grain boundary diffusion, Khalil *et al*. [39] also studied different point defects of Ag in SiC grain boundary [39]. The most energetically stable atomic configuration of Σ3-GB was determined by molecular dynamics (MD) simulations based on an empirical potential. A detailed description on the structure of Σ3-GB SiC is discussed in Section 3.1. The results of defect formation energies indicated that the Ag defects at the grain boundaries of SiC were approximately 2 to 4 eV lower than that in the bulk. It was found that Ag diffuses faster along the grain boundaries than through the bulk [39]. Also, at temperatures around 1873 K, Ag diffusion coefficients in grain boundary were found to be significantly higher than in the bulk, 3.7×10^{-18} m^2/s and 3.9×10^{-29} m^2/s, respectively [39]. Even though this diffusion coefficient in Σ3-grain boundary at 1873 K was about two orders of magnitude lower than that estimated from the IR measurements (show in

Table 1), the values were close enough to indicate that grain boundary diffusion was a possible diffusion mechanism of Ag release from SiC coating [39].

Shrader *et al*. [3] studied the diffusion of Cs atoms in bulk 3C-SiC. The most stable Cs defects in SiC, under n-type doping conditions, was found to be a negatively charged Cs atom substituting for a C atom and bound to two Si vacancies, Cs_C-$2V_{Si}^{-3}$ [3]. The Cs_C-$2V_{Si}^{-3}$ defect was found to have the lowest overall activation energy of roughly 5.14 eV, which agreed well with the values obtained from high temperature integral release experiments [1, 36]. It supports the hypothesis of bulk diffusion occurring at high temperatures, while grain boundary diffusion occurrs at lower temperatures [3]. In the present work, the diffusion of Cs at the ∑3-grain boundaries of SiC was investigated. The goal is to calculate Cs defect formation energies along the grain boundaries, which can then be used to calculate the activation energy and diffusion coefficient. By comparing the defect formation energies of Cs in the bulk and at the grain boundaries of SiC, the activation energies can be quantitatively predicted.

CHAPTER 3: COMPUTATIONAL DETAILS

3.1: Theoretical Approach

The total energies of the defected and un-defected SiC systems, using density functional theory calculations, were determined in the pseudo-potential formalism as implemented in Quantum ESPRESSO (open-Source Package for Research in Electronic Structure, Simulation, and Optimization) version CVS [40]. The generalized gradient approximation (GGA), parameterized by Perdew, Burke, and Ernzerhof (PBE), was used for estimating the exchange-correlation functional. There are two different material systems studied in this thesis: the bulk 3C-SiC and a SiC Σ3-grain boundary. The ultrasoft pseudo-potentials, generated using Vandebilt codes, were applied for carbon and silicon atoms in both systems [41]. For Cs, the pseudo-potential was generated as a norm-conserving pseudo-potential using Troulllier-Martins recipe. The pseudo-potentials for C and Si have 4 valence electrons in the $2s^2$ $2p^2$ and $3s^2$ $3p^2$ orbitals, respectively. The Cs's pseudo-potential has 0.6 electrons total in the valence states ($6s^{0.5}$ $5d^{0.05}$ $6p^{0.05}$) [41].

For calculations in bulk SiC, a wave function cutoff of 30 Ry and a charge density cutoff of 240 Ry were determined based on the convergence tests, which are shown in the next sections. A grid of Monkhorst-Pack 10×10×10 *k*-point mesh was used to sample the full Brillouin zone. These computational parameters yielded 4.381 Å (8.28 Bohr) and 210 GPa for the equilibrium lattice constant and the bulk modulus, respectively, which are in excellent agreement with the experimental values of 4.359 Å (8.24 Bohr) and 225 GPa

[42-43]. The relaxation calculations of the structure (e.g., lattice constant) and atomic positions were also carried out in order to obtain more optimized data of the total energies. All Cs defect calculations were done at the neutral charge state. To minimize the defect-defect interactions, a 2×2×2 super cell of the conventional un-defected SiC system containing 64 atoms was used in all calculations.

For investigating Cs in Σ3-grain boundary of SiC, a wave function cutoff of 44 Ry and a charge density cutoff of 352 Ry were applied for all calculations as proposed by Khalil *et al*. [39]. The atomic structure of the GB was generated using molecular dynamics simulations from the LAMMPS software package [39]. The grain boundaries were examined in a bicrystal configuration; the Σ3-grain boundary lies in the $[2\bar{1}\bar{1}]$ plane and its tilt axis is aligned with the $[0\bar{1}1]$ direction [39]. Figure 7 shows the XZ cross-sectional structure of the most stable Σ3-grain boundary, where it consists of 5-, 6-, and 7-membered rings. These rings are labeled in the figure as I, II, and III, respectively [39]. Also, in Figure 7, the Y direction of the Σ3-grain boundary is parallel to the tilt axis $[0\bar{1}1]$, while the X and the Z directions are $[111]$ and $[2\bar{1}\bar{1}]$, respectively [39].

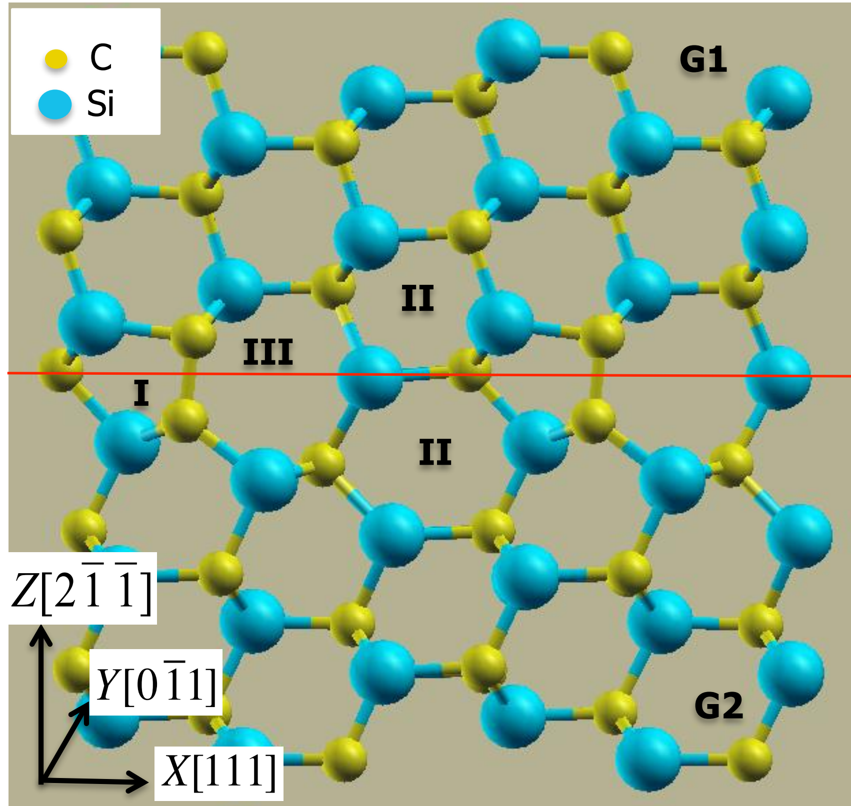

Figure 7 The XZ cross-sectional structure of the bi-crystal grain boundary model. The red line represents the grain boundary plane separating the grain 1 (G1) and grain 2 (G2). Only one layer of atoms is shown here while the others are into the page.

The lattice sites, overlapping between the two grains, form a periodic structure within the grain boundary plane, which is considered as a coincidence site lattice (CSL). The size of the CSL unit cell is 7.55 Å in X, 3.08 Å in Y [39]. The size of the whole grain boundary structure is 15.2 Å in X, 12.3 Å in Y, and 18 Å in Z directions [39]. An approximate thickness of 5 Å centered at the GB contains the atoms that form the GB rings. Other atoms, outside of this region, belong to the crystalline (bulk) SiC [39]. The dimensions are chosen in such a way that a reasonable number of bulk-like atomic layers could be incorporated around the grain boundary [39]. Applying the same grain boundary

structure given from Khalil *et al.* into this investigation, but using different integrating software (e.g., Quantum-ESPRESSO vs. VASP), it is required to obtain a new convergence with respect to the *k*-point mesh. The convergence test yielded a suitable 4×4×4 *k*-mesh for the calculations in the grain boundary of SiC. The Σ3-grain boundary calculations were computationally expensive (i.e., in time and memory) because it is a large system consisting of 256 atoms (128 Si and 128 C). Therefore, the relaxation of only atomic positions was done while its volume was fixed (e.g., fixed lattice constants). Similar to the bulk SiC calculations, defect formation energies were only studied with the neutral defects.

3.2: Defect Formation Energy

The defect energies of neutral Cs in two structural configurations of SiC were calculated using the following equation [30, 44]:

$$E_f = E_{def} - E_{undef} + \sum_i \Delta n_i \, \mu_i \qquad \textbf{[3.1]}$$

where E_{def} corresponds to the calculated total energy of the defected SiC system, E_{undef} is the calculated total energy of the un-defected cell, Δn_i is the difference in the number of atoms of species *i* between the perfect cell (defect free) to the defected cell, and μ_i is the chemical potential of species *i* [44].

The cohesive (or binding) energies were calculated via the total energies and further applied for the calculation of the defect energies. There were a total of 64, 2, and 4 atoms in the systems of bulk SiC, Si crystal, and C (graphite), respectively. The cohesive energies were calculated for SiC, Si, and C using the following equations:

$$E^a_{coh}(SiC) = \frac{E_{tot}(SiC_{bulk}) - 32 \times E(Si_{gas}) - 32 \times E(C_{gas})}{32} \qquad \textbf{[3.2]}$$

$$E^{a}_{Coh}(Si) = \frac{E_{tot}(Si_{bulk}) - 2\times E(Si_{gas})}{2} \quad \textbf{[3.3]}$$

$$E^{a}_{Coh}(C) = \frac{E_{tot}(C_{bulk}) - 4\times E(C_{gas})}{4} \quad \textbf{[3.4]}$$

where $E^{a}_{coh}(SiC)$, $E^{a}_{coh}(Si)$, and $E^{a}_{coh}(C)$ are the cohesive energies per atom (superscript a) of bulk SiC, Si, and C crystal. $E_{tot}(SiC)$, $E_{tot}(Si_{bulk})$, and $E_{tot}(C_{bulk})$ are the calculated total energies of the SiC, Si, and C bulk systems. $E_{tot}(Si_{gas})$ and $E_{tot}(C_{gas})$ are the total energy contributions resulting from isolated Si and C atoms [45], which were calculated as Si and C in their gas phase (e.g., in the present work, the calculations were performed using simple cubic structure with the lattice constant of 40 Bohr for both cases). The cohesive energies are used into the chemical potential calculation, which is important for defects that change the composition of the system. In pure SiC, the chemical potential of a Si-C pair in bulk SiC is denoted by μ_{SiC}. At equilibrium, μ_{SiC} is the binding energy (per pair of atoms) of SiC, which is equal to [45]:

$$E_{SiC} = 2\times E^{a}_{coh}(SiC) = \mu_{Si} + \mu_{C} = \mu^{bulk}_{Si} + \mu^{bulk}_{C} + \Delta \mathrm{H}f \quad [\textbf{3.5}]$$

where μ^{bulk}_{Si} and μ^{bulk}_{C} are the chemical potential of atoms in bulk Si and C (graphite) at equilibrium. $\Delta \mathrm{H}f$ is the heat of formation for the SiC compound. μ^{bulk}_{Si} and μ^{bulk}_{C} were considered under two extreme boundary conditions: C-rich and Si-rich [45]. The following procedure was used in order to obtain μ_{Si} and μ_{C}. For the Si-rich condition, μ_{Si} is at a maximum and equal to the energy of a Si crystal:

$$\mu_{Si} = \mu^{bulk}_{Si} = E^{a}_{Coh}(Si) \quad \textbf{[3.6]}$$

whereas μ_{C} is at a minimum and equal to the chemical potential of C in the SiC compound [45]:

$$\mu_C = \mu_C^{bulk} + \Delta \text{H}f = E_{SiC} - \mu_{Si}^{bulk} = 2\times E_{coh}^{a}(SiC) - E_{Coh}^{a}(Si) \quad \textbf{[3.7]}$$

Similarly, for the C-rich condition, μ_C is at a maximum and equal to the energy of bulk C (graphite):

$$\mu_C = \mu_C^{bulk} = E_{Coh}^{a}(C) \quad \textbf{[3.8]}$$

whereas μ_{Si} is at a minimum and equal to the chemical potential of Si in the SiC compound [30, 44]:

$$\mu_{Si} = \mu_{Si}^{bulk} + \Delta \text{H}f = E_{SiC} - \mu_C^{bulk} = 2\times E_{coh}^{a}(SiC) - E_{Coh}^{a}(C) \quad \textbf{[3.9]}$$

Along with calculating Cs defect formation energies, the intrinsic defect formation energies of Si and C vacancy in SiC systems were also calculated using the 2×2×2 conventional SiC super cell. The following equations were used in this thesis to determine the defect formation energy of a single vacancy in bulk SiC. They were consistent with the formula used by Posselt *et al.* [45]. For a single Si-vacancy:

$$E_f(V_{Si}) = E_{def} - E_{undef} - E_{Coh}^{a}(SiC) + E\left(Si_{gas}\right) + \frac{1}{2\left(E_{Coh}^{a}(Si) - E_{Coh}^{a}(C)\right)} \quad [\textbf{3.10}]$$

For a single C-vacancy:

$$E_f(V_C) = E_{def} - E_{undef} - E_{Coh}^{a}(SiC) + E(C_{gas}) + \frac{1}{2\left(E_{Coh}^{a}(C) - E_{Coh}^{a}(Si)\right)} \quad [\textbf{3.11}]$$

Note that the signs can be alternatively changed depending on whether the applied cohesive energy values are positive or negative.

In addition, the band structure and the density of states of bulk SiC were studied yielding band gap energy compatible with other computational works. The generalized gradient approximation exchange-correlation functional was used for these calculations.

The band structure was calculated and plotted for the primitive SiC system containing 8 atoms. The density of states calculations were done on the 2×2×2 conventional SiC unit cell containing 64 atoms. For all calculations of intrinsic and extrinsic defects in bulk SiC, a 2×2×2 conventional unit cell was used in order to reduce the interaction between defects and their periodic images.

3.3: Testing Convergence

3.3.1: Lattice Parameter and *k*-Point Convergence

In order to test the convergence of the lattice constant, *k*-point mesh, and the plane-wave cutoff energy for the accuracy of the SiC model and the software, several sets of self-consistent field calculations were done on the SiC conventional cell (8 atoms/cell) with various Monkhorst-pack *k*-point meshes including 2×2×2, 4×4×4, 8×8×8, 10×10×10, and 12×12×12. Throughout each *k*-point calculation set, the initial kinetic energy cutoff for plane wave function was used at 30 Ry, as proposed by Roma for SiC system [28]. The lattice constant was varied from 7.7 to 9.0 Bohr with 0.1 Bohr increments, which contained the experimental lattice constant of 3C-SiC (i.e., 8.24 Bohr). A typical result from calculating the total energy of 3C-SiC as a function of lattice constant is shown in Figure 8. The shape of the curve is quadratic and has a single minimum at a value of a, which is called a_o. Because materials always seek to minimize their total energy, DFT calculations predict that 3C-SiC has a minimum energy at lattice constant a_o.

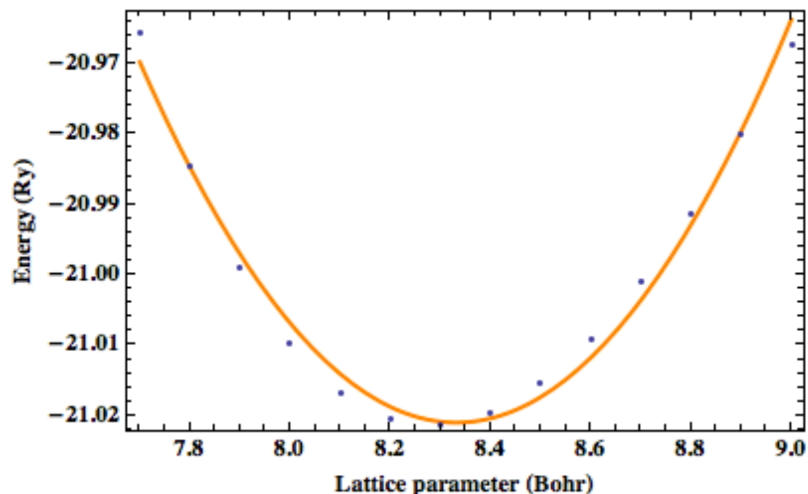

Figure 8 Total energy, of zinc-blend 3C-SiC structure, as a function of lattice parameter. The solid curve corresponds to the fit of DFT data. The plot was obtained using the Mathematica 8 program.

To extract the values of minimum total energy and a_o, the data were fitted using the NonlinearModelFit function of the Wolfram Mathematica program. The fit model was then solved for the minimum point, from which a_o can be determined. Alternatively, the Quantum-ESPRESSO package can calculate the bulk modulus, in which the minimum total energy and a_o can be obtained using the Murnaghan equation of state. Each set of *k*-point calculations produced one value of a_o and a minimum total energy. The data from each *k*-point calculation is given in the Table 2. First, looking at the energies listed in this table and plotted in Figure 9, when M is larger than 10, the total energy is almost independent of the number of *k*-points. More specifically, the variation in the energy (for M>10) is less than about 0.00001 Ry (~0.0001 eV). Similar behavior is seen for the lattice constants listed in the table and plotted in Figure 10. The variation in lattice constant is almost zero (due to rounding) as M approaches 10. These data indicate

that the calculations are numerically well converged at 10×10×10 *k*-points mesh when a_o equals to 8.281 Bohr.

The last column in Table 2 lists an average of the total computational time taken for the total energy calculations. It shows that getting a converged result, in a calculation that contains 47 *k*-points (M=10), takes approximately 4 times longer than the calculation involving just 3 *k*-points (M=2). The number of *k*-points in each *k*-mesh indicates the symmetries that exist in a perfect zinc-blend structure. The calculations take full advantage of these symmetries because the integrals in reciprocal space can be evaluated in a reduced portion of the Brilliouin Zone (i.e., the irreducible Brilliouin zone) instead of the entire zone [12]. For a very symmetric material such as cubic SiC, using just the irreducible Brilliouin zone would greatly reduce the numerical effort required to perform calculations.

Table 2 The results of the total energies and lattice constant computed with M×M×M *k*-points.

M	E_{total} (Ry)	a_o (Bohr)	No. of *k* Points in irreducible Brilliouin zone	Total CPU Time (s)
2	-20.84046	8.392	3	~2.12
4	-21.01203	8.285	8	~2.52
8	-21.02115	8.281	29	~4.79
10	-21.02123	8.281	47	~6.78
12	-21.02124	8.281	72	~9.49

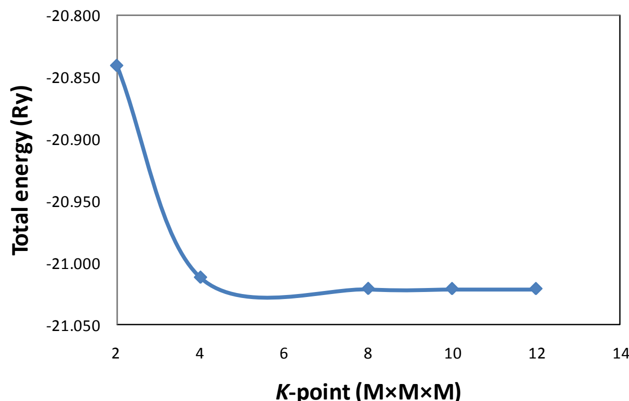

Figure 9 Total energy of SiC (as described in Table 2) plotted as a function of M for calculations using M×M×M *k*-points.

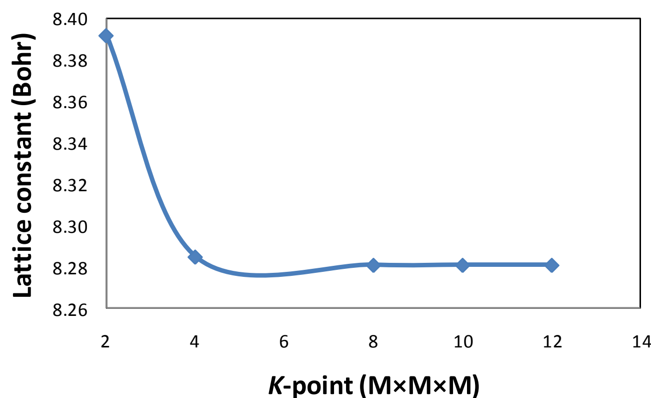

Figure 10 Lattice constant, as described in Table 2, plotted as a function of M for calculations using M×M×M *k*-points.

3.3.2: Kinetic Energy Cutoff for Plane Wave Function

The cutoff energy value was 30 Ry for all converging tests of *k*-points and lattice constants for SiC, as proposed by Roma [28]. However, for the purpose of consistency and accuracy, a convergence test for the kinetic energy cutoff was also performed in this thesis. With the *k*-point mesh of 10×10×10 and a_o of 8.281 Bohr, obtained from Table 2 and the figures above, the calculation was done using different cutoff values, from 20 to 40 Ry. The result is shown in Figure 11, in which the variation of the total energy

becomes very small after the cutoff value reaches 30 Ry. The figure indicates that 30 Ry is a reasonable choice for the energy cutoff value in SiC calculations. As a result, all further calculations of the bulk SiC were done using 30 Ry as the cutoff energy.

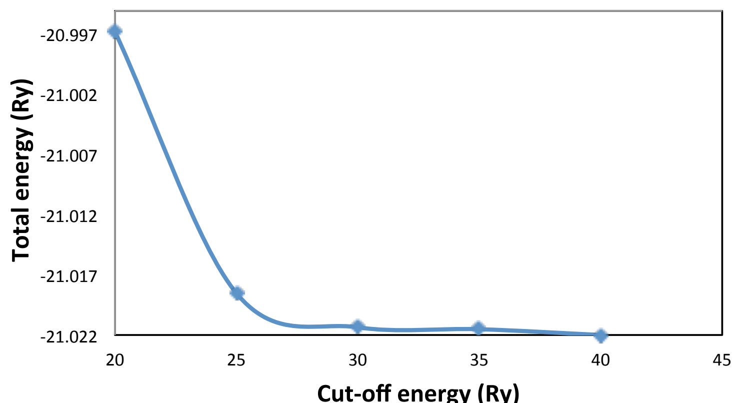

Figure 11 The total energy of the bulk SiC calculated as a function of kinetic cutoff energy.

After the suitable *k*-points, the lattice constant, and the energy cutoff data were optimized for the calculations in bulk SiC system containing 8 atoms per cell, calculations of the larger SiC system were performed using the super cell, which contains 64 atoms. The 2×2×2 bulk SiC super cell was used for defect calculations to prevent the contribution of defect-defect interaction from the calculation of formation energy.

For the calculations in the grain boundary SiC, the convergence test was done only for the *k*-points, because the lattice parameters and the kinetic energy cutoff were used as previously determined by Khalil *et al*. [39]. Using these parameters for the calculations with different *k*-points, the result of the total energies plotted as a function of *k*-points is shown in Figure 12. In this system, the energy becomes almost independent of

the *k*-points (M×M×M) as M reaches 4. Hence, the mesh of 4×4×4 *k*-points was used for all further calculations of grain boundary SiC.

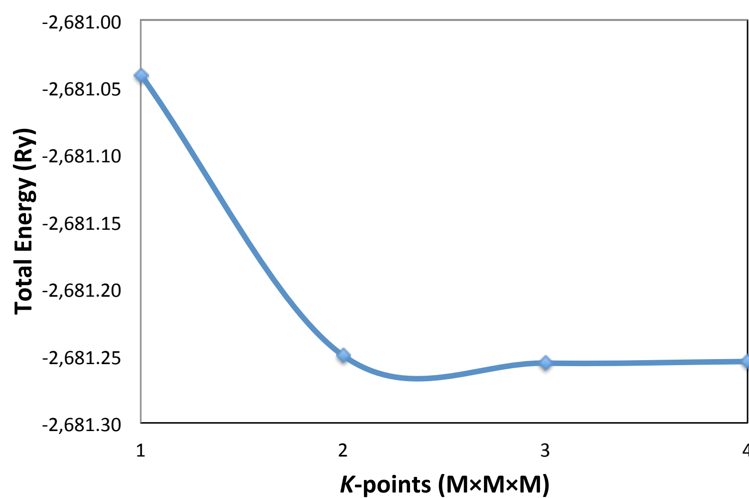

Figure 12 The total energy of grain boundary SiC plotted as a function of *k*-points.

CHAPTER 4: RESULTS AND DISCUSSION

The ultimate goal of this thesis is to understand the diffusion mechanism for Cs in SiC, whether the diffusion occurs in the bulk or at the grain boundaries. In order to achieve the end result, many challenges have to be overcome. One challenge is to understand the fundamental concepts of density functional theory before implementing it into simulations. Another is to perform baseline calculations using the Quantum-ESPRESSO software package, including the determination of the total ground state energy, the density of states, the band structure, and the charge density. This investigation was begun with several neutral Cs point defects such as interstitial, substitution, and the combination of vacancy plus substitution, before gradually moving into more complex charged defects.

4.1: Bulk 3C-SiC

Once the lattice constant, the kinetic energy cutoff, and the *k*-point mesh were determined for bulk SiC system, these parameters could be applied for all of the bulk SiC calculations. The primary parameters used in this thesis are listed in Table 3. However, to gain more confidence on using these data on the calculations, several different material properties such as the bulk modulus and the cohesive energy of bulk SiC were also studied. The results of bulk modulus and cohesive energy are shown in Table 4. The experimental data and data from other simulation works are also listed in Table 4 for the convenience of comparison.

Table 3 Primary parameters for calculations in bulk 3C-SiC with 1×1×1 and 2×2×2 super cells

SiC system	Wave function cutoff energy (Ry)	Charge density cutoff energy (Ry)	Lattice constant (Bohr)	*k*-point
8 atoms/cell	30	240	8.28	10×10×10
64 atoms/cell	30	240	16.56	5×5×5

Table 3 shows that the values of kinetic energy cutoff for plane wave function and charge density are constant whether it is the 1×1×1 SiC unit cell or it is a 2×2×2 SiC super cell. The value of the charge density cutoff energy was used as 8 times the value of the wave function cutoff energy for any calculations that used the ultra-soft pseudo potentials, as proposed by Paolo Giannozzi [46]. The lattice constant of the SiC super cell was double the value found for the simple unit cell. The M *k*-points were also determined as 5×5×5 for the SiC super cell based on the data obtained from simple unit cell calculations.

Table 4 shows that the values obtained from this thesis are in good agreement with the previous calculations as well as the experimental data. The variation among different calculations can be due to the difference of exchange-correlation functional approximation, the lattice constants, *k*-point, the kinetic energy cutoff values, and the simulation software. The calculated SiC properties yielded a great confidence for applying the parameters determined in Table 3 and gave more assurance on the accuracy of the SiC future calculations.

Table 4 Equilibrium lattice constant, Bulk modulus, and cohesive energy with respect to the calculation method and *k*-points

Reference	Present work	Exp.[43]	[47]	[29]	[48]	[49]	[43]	[50]	[51]
a_o (Bohr)	8.28	8.24	8.24	8.28	8.28	8.27	-	8.21	8.22
Bulk Modulus (GPa)	210	225	210	-	222	213	227	222	224
E-coh (eV/atom)	7.51	6.34	-	7.32	6.58	-	7.55	-	-

Next, the electronic band structure of 3C-SiC was also investigated at the high symmetry points of the zinc blende Brilliouin zone. The result in Table 5 shows that the electronic band gap energy for SiC in zinc-blende crystal structure in this present work was found to be 1.40 eV, which is comparable with other theoretical data that used a similar computational approach (i.e., 1.37 eV and 1.53 eV [50, 52]). In addition, Figure 13 illustrates an indirect band gap from the Γ-point (000) to the X-point (100), which agreed with the experimental data [53]. Figure 13 also shows the Fermi level at zero, which had been normalized by subtracting the energy with the Fermi energy value to make it a reference energy level. The conduction and the valence bands are defined as the nearest energy states above and below the Fermi level, respectively. The band gap energy was measured from the top of the valence band, at the zone center (Γ point), to the bottom of the conduction band at the X-axis.

Table 5 Band gap energy of 3C-SiC based on density functional theory calculations in comparison with the experimental data

	Present work	[50]	[52]	[30]	[54]	[55]	Exp.[26]
E-gap (eV)	1.40	1.37	1.53	1.07	1.501	1.32	2.39

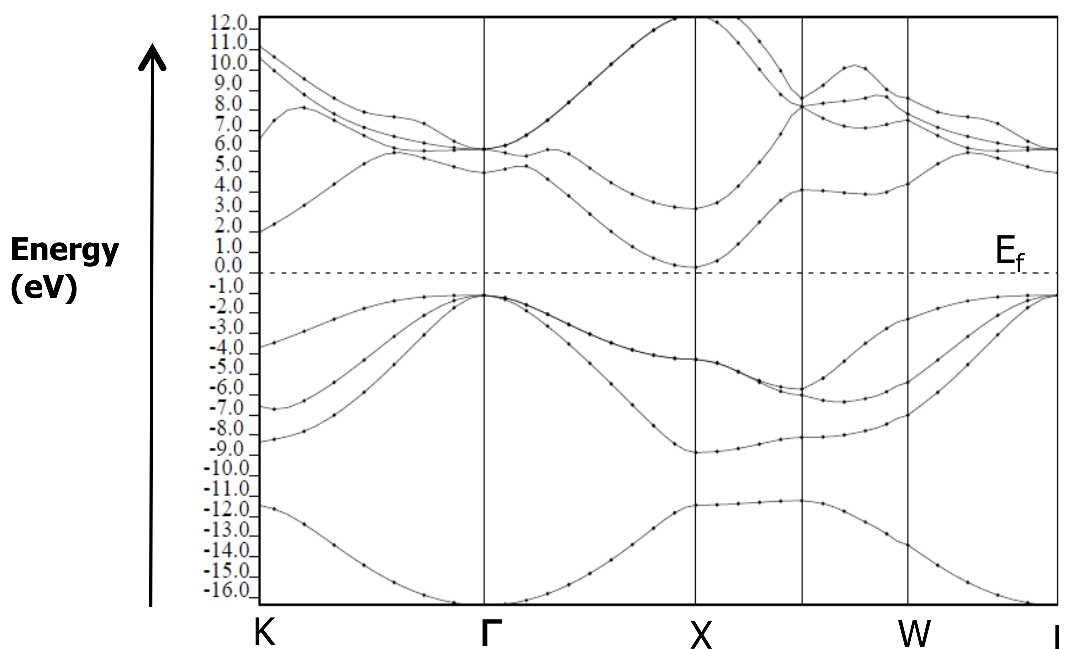

Figure 13 Band structure of 3C-SiC calculated at the equilibrium volume. The Fermi level is taken as the zero of energy.

The band gap energy of 1.40 eV calculated for 3C-SiC was in good agreement with other calculations, but was low compared to the experimental data. The tendency of density functional theory to underestimate the electron-electron interactions causes DFT calculations (of different exchange-correlation functional) to suffer a self-interaction error, resulting in lower electrical band gap energy than the actual value [11]. There are several band gap correction methods that can improve the performance of DFT

calculations on determining the band gap energy of materials. A great review on these correction methods can be found in Ref. [56]. According to Gali [11], the band gap error in wide-band-gap semiconductors, like 3C-SiC, was quantitatively analyzed as roughly 1.0 eV [11]. Therefore, the energy band gap of 1.40 eV found in this was not only consistent with other calculations but also in good agreement with the experimental data. Moreover, the results imply that the parameters used for bulk SiC calculations were reliable.

4.2: Cs in Bulk 3C-SiC

As proposed by Shrader *et al.* [3] and Roma [28], the SiC 2×2×2 super cell was used for all defect calculations to prevent the defect-defect interaction. Three Cs point defects, including Cs interstitial at the octahedral site, and Cs substitution on the Si (or C) sub-lattice, were chosen as the initial calculations. The crystal structures of different Cs point defects in SiC are shown in Figure 14. Due to the large atomic size of Cs (atomic radius of 2.67 Å (5.05 Bohr)) in comparison with Si and C (atomic radii of 1.32 Å (2.50 Bohr) and 0.91 Å (1.72 Bohr), respectively), a significant distortion in the lattice surrounding the Cs defect would cause the lattice constant of the bulk SiC to change. In this investigation, to ensure that the lattice distortion was considered in each defect calculation, several sets of self-consistent field calculation were done within a lattice constant ranging from 15.5 Bohr to 17.5 Bohr. This range includes the 16.56 Bohr of the equilibrium lattice constant for the bulk SiC 2×2×2 super cell (Table 3).

For each defect, the new equilibrium lattice constant was then determined by fitting the total energy versus lattice constants to the Murnaghan equation of state. The data in Table 6 indicates that the equilibrium lattice constant of bulk SiC increased as a

result of Cs impurities. Additionally, among the defects, Cs substituting for C caused the least distortion in the lattice (0.24 Bohr from the equilibrium bulk lattice constant), which may suggest that Cs prefers the C sites over the Si and the interstitial sites, as its large atomic size is easier to be accommodated. However, more evidence from the defect formation energies is needed to validate this hypothesis. Due to the lattice distortion, all Cs defect calculations were then performed with the new equilibrium lattice constant depending on the defect type. At the same time, the variable cell relaxation method of calculations, in which the atomic positions and the lattice parameter(s) were both relaxed, were used to further reduce the ground state total energy for SiC system.

Table 6 Theoretical lattice constants of 3C-SiC with and without Cs point defects

Material system	a_o (Bohr)
bulk 3C-SiC	16.56
Cs substitution C	16.80
Cs substitution Si	16.96
Cs interstitial	16.98

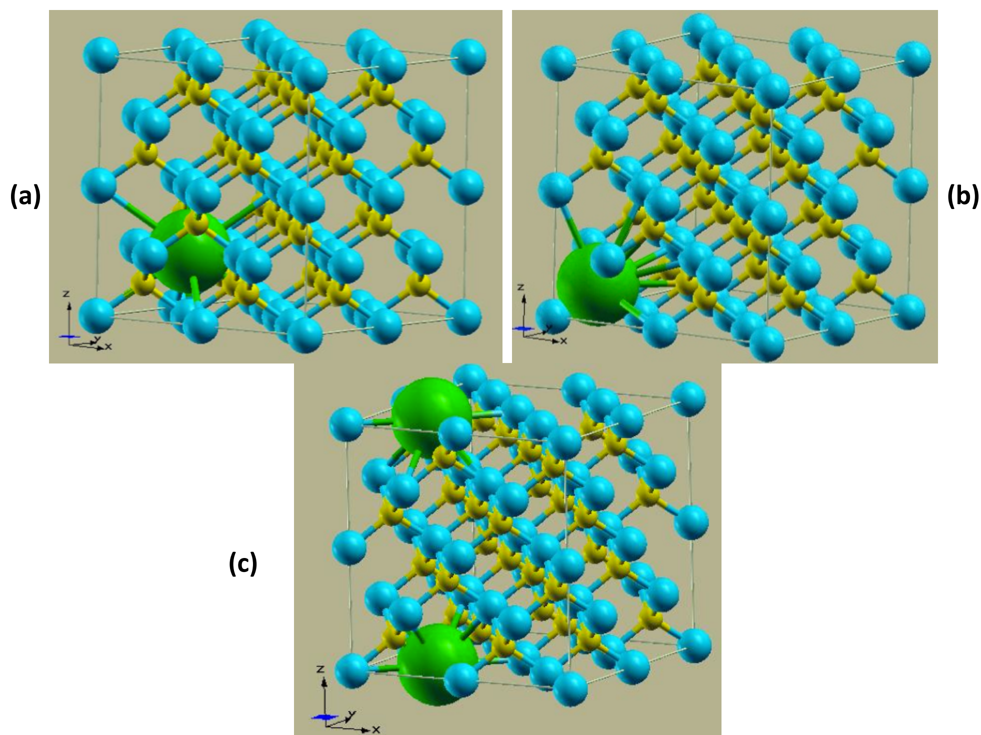

Figure 14 Crystal structure of Cs interstitial at the octahedral site (a), Cs substitution C site (b), and Cs substitution Si site (c).

4.2.1: Charge Distribution

In order to predict the probability of finding the location where the electron density will be the highest, the charge density calculations were carried out for both defect-free and defected SiC systems. From these calculations, the amount of charge being transferred from one atom to another can also be determined. The charge distributions were only taken in the (110) plane, which contains the most information of different Cs defect types. For the defect-free SiC, the charge distribution is shown in Figure 15. The partial density of states output file showed that there were roughly 1.00 electrons being transferred from the Si to the C atoms. The Si-C bond in 3C-SiC is sp^3 hybridized. In this case, the electronegativity of C is much higher than that of Si (2.55 and 1.90 respectively), and electro-negativity is the tendency of an atom to attract an electron to its nucleus. This difference caused the transfer of charge from Si to C to

occur. Figure 15 shows an uneven charge distribution in the Si-C bond along the (110) plane. The result verified, as expected, what has been reported on the bonding characteristic of Si and C atoms in 3C-SiC [2, 43, 51]. Additionally, Figure 15 shows almost no interaction of the C and the Si atoms in between the layers (separated as red). The charge transfer between the atoms can also be described based on Coulomb's law [57], which defines the attraction force between the two atoms as follow:

$$F = \frac{k\, q_1 q_2}{d^2} \qquad \textbf{[4.1]}$$

where F is the attraction force, q_1 and q_2 are the charges of the atoms, and d is the distance between the atoms. With that being said, the distance between the C and Si atoms were too far away, roughly 3.64 Å (6.88 Bohr) (Figure 15), thus almost no electrons were being transferred from Si to C atoms between different layers.

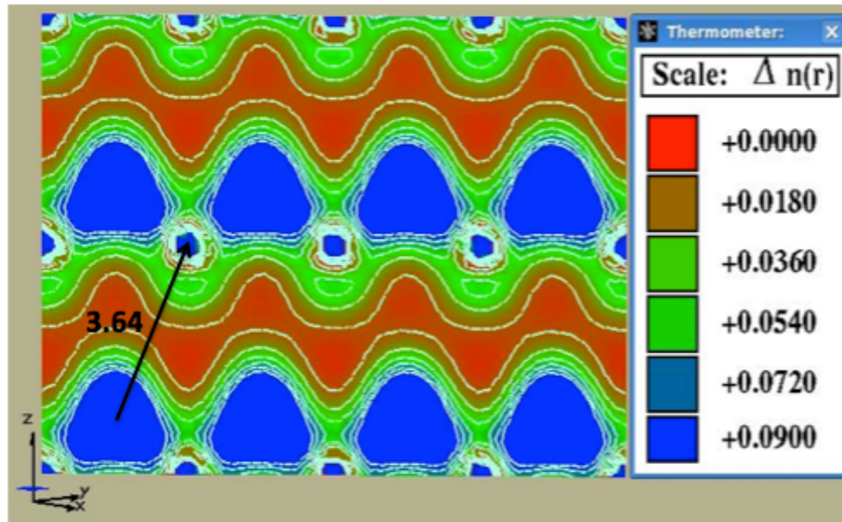

Figure 15 Charge density of bulk 3C-SiC along the (110) plane.

Once the charge density along the (110) plane was established for the defect-free 3C-SiC system, similar calculations were done with several Cs point defects. Shown in

Figure 16 is the charge density along (110) plane for Cs sitting on the C site (a), Cs sitting on the Si site (b), and Cs sitting on the interstitial site (c). The vertical direction of Figure 16c was taken as [002] instead of [001] in the z direction so that a full observation of charge distribution around the Cs atom can be seen.

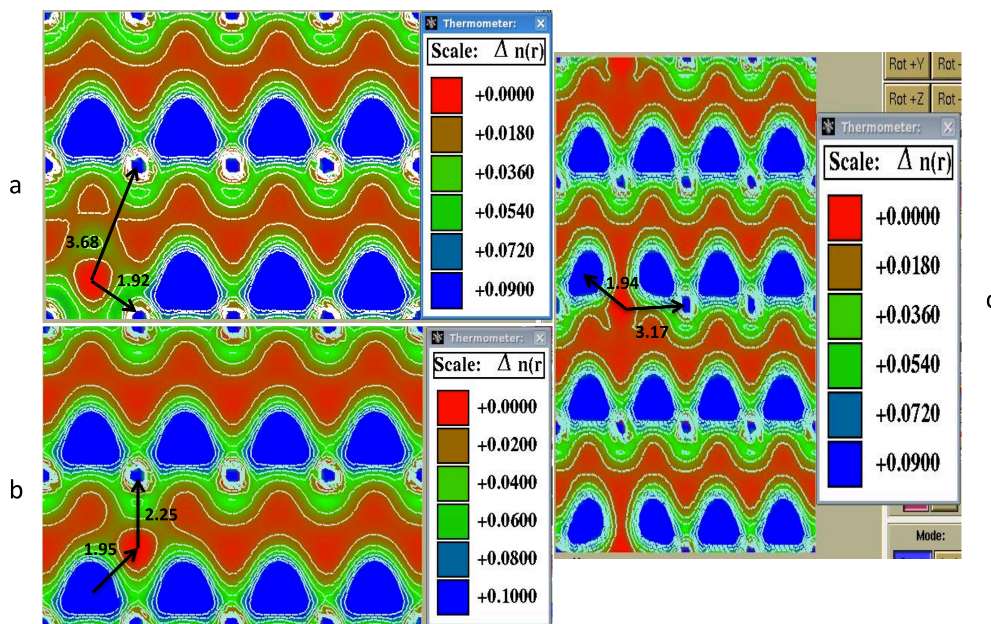

Figure 16 The charge density along the (110) plane of the Cs point defects in 3C-SiC system: Cs_C (a), Cs_{Si} (b), and Cs_i (c).

The images show that there are interactions between Cs with its surrounding Si and C atoms. For example, in Cs_C defect (Figure 16a), at the region where there was no sign of interaction (e.g., zero charge density) in the defect-free SiC (Figure 15), it is now showing some charges accumulated around the Cs atom. In comparison to the defect-free SiC charge distribution, the C-Si bond length and Cs-Si bond length between different layers (separated as red in the figures) are very close in both cases (3.64 Å (6.88 Bohr) and 3.68 Å (6.95 Bohr) in Figure 15 and 16, respectively), but Cs is a much larger atom than C, thus the nuclear effective charge on the valence electrons are weak and they can

easily interact with other surrounding atoms. Normally, it is expected that the atom with higher electronegativity will attract an electron to its nucleus. For example, Si (or C) will pull electrons from Cs to their side because Cs has much lower electro-negativity (e.g., 0.569). However, the results from charge density calculations of Cs defects showed an opposite behavior in this investigation. The valence electron configuration used for the pseudo-potential of Cs atom was $6s^{0.5}$ $5d^{0.05}$ $6p^{0.05}$, and the charge density output indicated a large amount of electrons being transferred from Si (or C) atoms to Cs in all cases. In the case of Cs_C, this behavior can be explained due to the dangling bond around Si when C was replaced with Cs. One of the Si bonds was unfulfilled, while the other three were bonded with C atoms. Because Si and C have 4 electrons in their valence, in the absence of a C atom, Si had one broken bond, which needed another electron to generate a single stable bond. When Cs was present with a low number of valence electrons (0.6 electrons) and empty energy states, the Si atom gave away its electron to fulfill the empty states of Cs, instead of taking 0.6 electrons from Cs. Therefore, the Si-Cs bond behaved like an ionic bond. Similar result can also be observed for C-Cs bond when Cs replacing Si atom. From the partial density of states output file, a summary of the charge transfer data to the Cs atom with respect to the s, p, and d orbitals and the overall charge gained to Cs are reported in Table 7. The initial charge configuration of Cs (containing the initial charge of 0.6 electrons) is also listed in Table 7.

Table 7 Data of electrons gained to the s, p, and d orbitals of Cs atom in each defect type.

Defect System	Cs initial electron configuration	*s* orbital	*p* orbital	*d* orbital	Total electrons gained to Cs atom
Cs_C	$[6s^{0.5}5d^{0.05}6p^{0.05}]$	0.268	0.617	4.28	~5.16
Cs_{Si}	$[6s^{0.5}5d^{0.05}6p^{0.05}]$	0.225	0.649	2.72	~3.59
Cs_i	$[6s^{0.5}5d^{0.05}6p^{0.05}]$	0.336	0.638	3.72	~4.69

From Table 7, the overall charge values of Cs indicate that Cs gained electrons from its surrounding Si and/or C atoms depending on the defect type. Based on the data collected, the electrons mainly resided in the 5d energy states. Table 7 also shows some loss of electrons in the s orbital. The electrons are believed to be transferred into a more localized 5d orbital resulting from the 6s to 5d hybridization in Cs atom [58]. The unoccupied 5d orbital of Cs was strongly hybridized resulting in more energy states generated within the band gap of SiC. More information on the hybridization in Cs atoms can be found in [59] and [60]. In addition, the calculations for the density of states were performed showing the hybridization process of the Cs atom's 5d orbital with the conduction band minimum and valence band maximum energy states.

4.2.2: Density of States

As discussed in Section 4.2.1 regarding the simulation process of charge distribution, a similar approach was taken for the density of states calculations, where the density of states of the defect-free SiC was performed prior to the defected SiC. The plot of bulk 3C-SiC density of states as a function of energy is shown in Figure 17. The Fermi level was normalized at zero. The conduction band minimum and the valence band

maximum were then determined based on this zero reference point. The band gap, 1.40 eV, obtained from the plot of the density of states was consistent with what was found from the band structure (Figure 13).

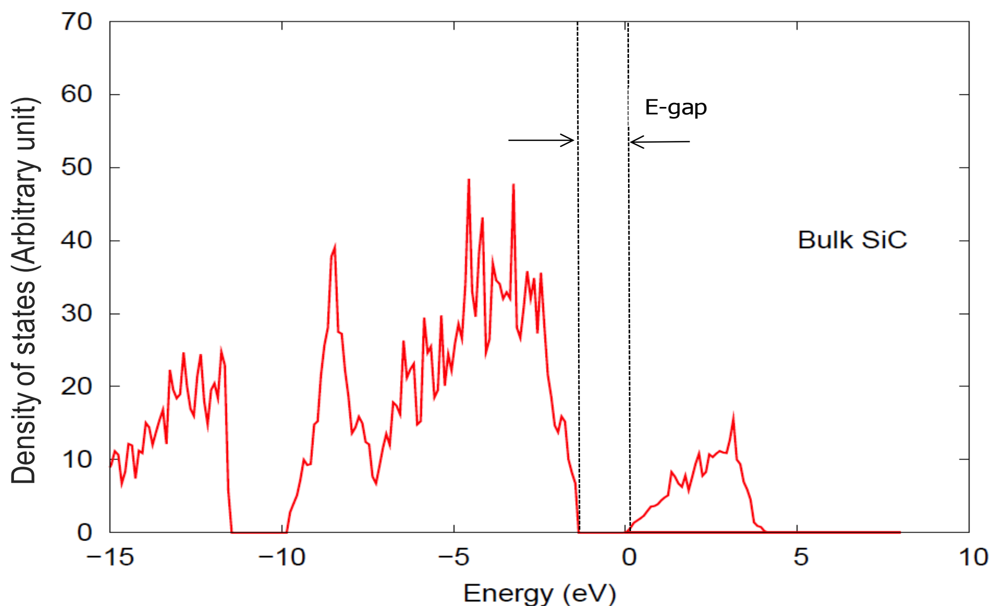

Figure 17 Density of states as a function of energy for bulk 3C-SiC. The band gap energy is indicated as E-gap and the Fermi level is at zero.

The calculations for the density of states of three different Cs point defects were performed. The results are shown in Figure 18. The density of states of the bulk 3C-SiC was also shown along with the density of states of the defects including Cs_C, Cs_{Si}, and Cs_i in parts (a), (b), and (c), respectively. In Figure 18a, there is an additional peak within the band gap at 0 eV when Cs was introduced into SiC at the C site. Furthermore, the partial density of states for the 5d orbital of Cs was also collected and plotted against the total density of states for the bulk and Cs-defected SiC. In Figure 19a, the 5d orbital of Cs also exhibits a matching peak at 0 eV similar to the peak shown in the defect's density of

states. This peak was broadened due to the hybridization the 5d orbital of Cs with the conduction band minimum and valance band maximum causing additional energy states to form in the SiC band gap. New energy states allow electrons to easily migrate from the valence band to the conduction band, resulting in a potential enhancement of the electrical conductivity in SiC.

The valence electron configuration model of $6s^{0.5}$ $5d^{0.05}$ $6p^{0.05}$ used for the pseudo-potential of Cs worked well for the Cs_C defect. Therefore, it is expected that an additional peak will occur and will also match with a peak resulting from the partial density of states of the 5d orbital of the Cs atom in the other two defects. However, for Cs_{Si} and Cs_i, shown in Figure 18b and 18c, respectively, the plots indicate a different behavior as in the Cs_C defect. In Figure 18b, the partial density of states of the 5d orbital of Cs shows a peak at roughly 4 eV while the total density of states of the defected SiC has a peak around -0.5 eV within the band gap. Similarly, in Figure 18c, the partial density of states of the 5d orbital of Cs shows a peak at roughly 1 eV, where the total density of states does not show any additional peak within the band gap. Based on these results, the current model of electron configuration used in Cs pseudo-potential may need to include some additional inner states to provide more valence electrons.

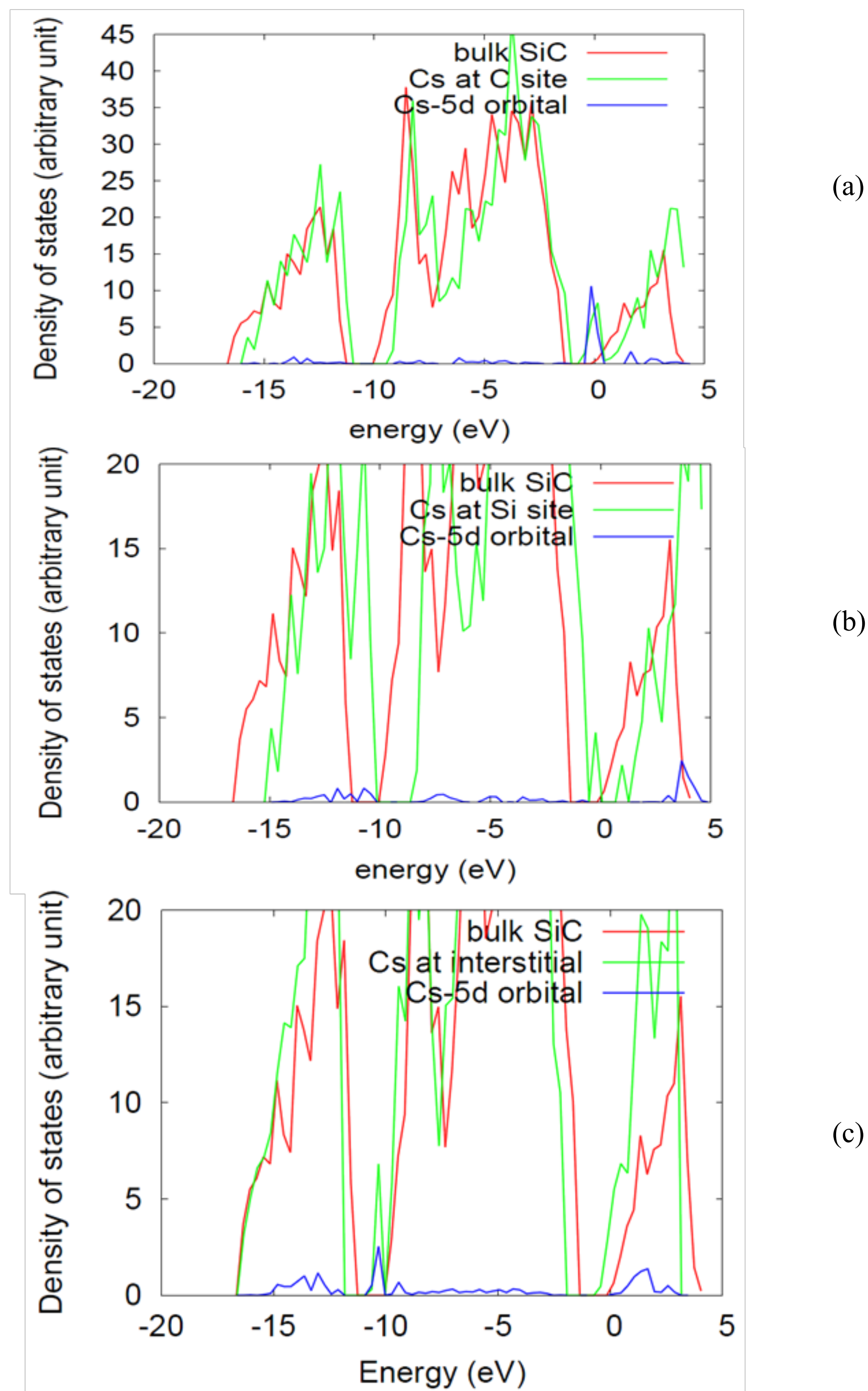

Figure 18 Total density of states of 3C-SiC with and without Cs defects along with the partial density of state of Cs's 5d orbital, where (a) is Cs_C, (b) is Cs_{Si}, and (c) is Cs_i.

4.2.3: Defect Formation Energy

In this subsection, the defect formation energies of isolated Cs impurities in 3C-SiC were calculated. Following the calculation approach as proposed by Shrader *et al.* [3], Cs point defects in bulk SiC are considered for three single and five complex defects. The single defects are Cs interstitial and substitutional impurities. The complex defects are formed by a Cs substitution in association with one to three vacancies of either C or Si atoms. Before evaluating the defect energies, the chemical potentials of Si and C were calculated in the bulk and in the SiC compound environments.

4.2.3.1: Chemical Potential of Si and C

In a material system, many defect reactions involve exchanging atoms or electrons with an external resource, which is stabilized and governed by a chemical potential [30]. Therefore, for the study in SiC, the defect formation energy depends upon the external chemical potential of Si and C (incorporated in Eq. 3.1). The Si and C chemical potential cannot be higher than the values of the bulk phases (bulk silicon and graphite, or Si-rich and C-rich); otherwise, these bulk phases will form spontaneously and will reduce the chemical potential [30]. In thermodynamic equilibrium, the chemical potential of Si and C are related to the chemical potential of the SiC crystal (discussed in Section 3.1). These are the constraints that provide the upper and lower bounds on the Si and C chemical potential [30]. Furthermore, the Si- and C-rich conditions are the bounds by which the formation energies of defects are allowed to vary. In the present study, the relevant binding energies of Si, C, and SiC were used for calculating the chemical potential of Si and C with respect to the chemical potential of SiC. These binding energies are shown in Table 8, which were calculated using Eq. 3.2, Eq. 3.3, and Eq. 3.4.

The values were consistent with a previous study, which used a similar DFT calculation method (general gradient approximation) [43]. The results of chemical potential in Si- and C-rich conditions are reported in Table 9 and were consistent with the data reported by Shrader *et al.* [30].

Table 8 The binding energy of Si, C, and SiC compound

	Binding energy (eV)
Si	5.398
C (graphite)	9.233
SiC (per pair of atoms)	15.02

Table 9 Chemical potential of Si and C atoms in Si-rich and C-rich conditions compare with data reported from Shrader *et al.*

	Present work		[30]	
	μ_{Si} (eV)	μ_C (eV)	μ_{Si} (eV)	μ_C (eV)
Si-rich	-5.39	-9.63	-5.44	-9.65
C-rich	-5.79	-9.23	-5.89	-9.20

4.2.3.2: Defect Formation Energy Calculation

The intrinsic defects are the common defects in most materials, and diffusion processes for impurities are often mediated by vacancies. It is useful to understand the properties of the host material itself. Therefore, in this investigation, the intrinsic defects in SiC were first investigated. At the same time, by comparing the results in this study with the existing literature will give more confidence in the methodology used in the present work (e.g., the pseudo-potentials, the Quantum-ESPRESSO codes, and other parameters discussed in Section 3.3). The calculations for the total ground state energy of

3C-SiC with a single vacancy of Si and C atoms were performed. The total energies were then used in Eq. [3.10] and Eq. [3.11] to calculate the vacancy formation energies. The results are given in Table 10. Relevant theoretical data from other works are also shown in Table 10, and are generally in good agreement with the present results. The data shows that it requires more energy to create a single Si vacancy than a single C vacancy in 3C-SiC, as expected, because Si has larger atomic size than a C atom causing greater distortion upon its removal. This can also lead to higher formation energy for Cs_{Si} than for Cs_C. This was indeed observed from the results of Cs defect formation energies (Table 11).

Table 10 Intrinsic defect formation energies (eV) for Si and C vacancy in 3C-SiC

Intrinsic defect	Present work	[48]	[49]	[61]	[62]	[30]
V_{Si}	7.62	7.62	6.64	7.48	7.01	7.63
V_C	4.38	3.47	5.48	3.63	4.89	4.13

The calculations of Cs defects in SiC were performed with the atomic and structural relaxation. The total energies for three neutral Cs point defects including Cs interstitial, Cs substitution for Si atom, and Cs substitution for C atom were first obtained. For calculating the defect formation energies (Eq. 3.1), E_{def} energy corresponding to the relaxed cell (Table 6) were used (i.e., the different lattice constant was used for different defects). The results are listed in Table 11. It shows that Cs substituting at C requires lower energy than Cs substituting Si. It is now verified that Cs prefers to sit at the C site. Interestingly, Cs interstitial at the octahedral site has much higher defect formation energy than Cs substitutional defects, indicating that Cs sitting at

the interstitial site is not energetically favorable. Table 11 also listed the calculated defect energies for neutral Cs-vacancy clusters in bulk SiC. The data of similar Cs neutral defects reported by Shrader *et al.* [3] are also given in Table 11. The results were generally in good agreement and the trend in defect formation energies of all defects is the same in between the works. The difference between the two data sets is due to the difference in pseudo-potentials and other parameters used in calculations.

In both studies, the exchange-correlation was treated in the Generalized Gradient Approximation (GGA) parameterized by Perdew, Burke, and Ernzerhof (PBE). However, in the present study, the pseudo-potential formalism was used for all calculation, while Shrader *et al.* [3] used the projector-augmented plane-wave (PAW) formalism. In Ref. [3], the PAW potential of Cs were used with valance electronic configurations $5s^2$ $5p^6$ $6s^1$, while the norm-conserving pseudo-potential of Cs contained only 0.6 valence electrons in the configuration of [$6s^{0.5}$ $5d^{0.05}$ $6p^{0.05}$], which is used in the present investigation. There was only one Cs pseudo-potential available from the pseudo library of the Quantum-ESPRESSO. Meanwhile, a lot of work is required to generate a Cs pseudo-potential with different valence electron configuration. In fact, it was generated during this research, but in comparison with the calculations using the Cs pseudo-potential from the Quantum-ESPRESSO package, the testing result for the Cs bulk modulus was not as accurate as expected. As a result, the available pseudo-potential from the Quantum-ESPRESSO package was used in this investigation, which contains 0.6 valence electrons [$6s^{0.5}$ $5d^{0.05}$ $6p^{0.05}$].

In addition, for the work in Ref. [3], the Brillouin Zone was sampled using the Monkhorst-Pack *k*-points mesh of 6×6×6 for an 8-atom conventional SiC cell (1×1×1

unit cell), and the Fourier space *k*-points density was used for different cells (e.g., 6×6×6 k-mesh in 1×1×1 unit cell will be converted to 3×3×3 k-mesh in 2×2×2 super-cell). The kinetic energy cutoff for wave functions was set to 600 eV (~44 Ry) for all of their calculations [3]. In this study, the 10×10×10 *k*-points was used for the calculations of the unit cell containing 8 atoms and the 5×5×5 *k*-points was used for the super cell containing 64 atoms. Also, the kinetic cutoff energy in this study was set to ~408 eV (30 Ry).

Nevertheless, there is a good agreement in the trends for defect energies between the two investigations. Both studies predicted that the most stable neutral Cs defect was the Cs substituting Si site in association with a C vacancy (bold values). Thus, despite some differences in the calculated defect energies, the results from the present work provided enough confidence for the future investigations of Cs at the grain boundary in SiC.

Table 11 Defect formation energies of neutral Cs defects in bulk 3C-SiC under the two boundary conditions of the chemical potential: Si-rich and C-rich.

Cs defect	Chemical potential boundary condition	Present work (eV)	Shrader *et al.* for Cs defect [3] (eV)	Ag defect	Shrader *et al.* for Ag defect [30]
Cs_{Si}	Si-rich	14.58	12.71	Ag_{Si}	6.60
	C-rich	14.19	12.27		6.16
Cs_{C}	Si-rich	12.07	12.50	Ag_{C}	7.39
	C-rich	12.46	12.94		7.83
Cs_{i}	Si-rich	26.55	23.46	Ag_{i}	10.49
	C-rich	26.55	23.46		10.49
Cs_{Si}-V_{C}	**Si-rich**	**11.97**	**10.93**	Ag_{Si}-V_{C}	**5.32**
	C-rich	**11.97**	**10.93**		**5.32**
Cs_{Si}-2V_{C}	Si-rich	12.37	11.39	Ag_{Si}-2V_{C}	6.44
	C-rich	12.76	11.84		6.88

Cs_C-2V_{Si}	Si-rich	13.87	13.59	Ag_C-2V_{Si}	11.40
	C-rich	13.48	13.15		10.96
Cs_{Si}-V_C-C_{Si}	Si-rich	13.81	12.95	Ag_{Si}-V_C-C_{Si}	8.56
	C-rich	14.59	12.07		7.67
Cs_C-V_{Si}-Si_C	Si-rich	16.76	13.74	-	-
	C-rich	15.98	14.62		-

Table 11 also shows the formation energies of similar neutral Ag defects in bulk 3C-SiC, which were calculated by Shrader *et al*. [30]. Notice that the last Ag defect is not listed in Table 11 because it was not studied in their work. Looking at defect formation energies of Cs in the present work and of Ag from Ref. [30], both show that the defect cluster of Cs (Ag) substituting a Si atom in association with a C vacancy has the lowest values. It indicates that the most probable stable state of neutral Cs and Ag defects in bulk SiC is this defect cluster. Also, at the interstitial site, both Cs and Ag defects have very high formation energies suggesting that it is not energetically favorable for Cs and Ag to sit at the interstitial in bulk SiC. In general, the formation energies of Ag defects are smaller than Cs defects. Because Ag is much smaller than a Cs atom (1.44 Å (2.72 Bohr) and 2.67 Å (5.21 Bohr), respectively), it is easier to transport with less disruption to the structure of the host material, bulk SiC. Therefore, it would require less energy to form Ag defects in SiC because with smaller size Ag is more compatible with the SiC than Cs.

4.3: Cs at Σ3-Grain Boundary SiC

Table 1 containing the experimental data of Cs diffusion in SiC indicates a change in the mechanism of Cs diffusion in SiC at temperatures around 1673 K. Shrader *et al.*

studied Cs diffusion in bulk 3C-SiC for different neutral and charged defects [3]. They also hypothesized that Cs is more likely to diffuse through the grain boundaries of SiC at the temperatures below 1673 K [3]. Even though the activation energies predicted by Shrader *et al.* were consistent with the high-temperature release measurements, the formation energies indicated an extremely low Cs solubility [3] in bulk SiC. Therefore, Shrader *et al.* proposed that other diffusion mechanisms must be investigated to provide a better understanding on the solubility of Cs in SiC [3]. However, there has been no investigation to support the hypothesis until this present work, where all calculations at the grain boundary were obtained by using the relaxation method. The formation energies were first calculated for the intrinsic defects along the grain boundary of SiC to verify the theoretical data from Khalil *et al.* [39]. Then, the calculations of neutral Cs substitutions in place of the intrinsic defects were performed for their ground state total energies. Due to the small difference of the Si (C) chemical potential in the Si-rich and C-rich conditions (~0.39 eV), only the chemical potential in the Si-rich condition is being used for defect formation energies calculation.

4.3.1: Intrinsic SiC Defect Energies

There were a total of six single vacancies studied in this research. These defects include a vacancy at the grain boundary plane, a vacancy in grain 1 (above the grain boundary plane), and a vacancy in grain 2 (below the grain boundary plane) for both C and Si. Figures 19 and 20 show the single C and Si vacancies in the crystal structure of the Σ3-grain boundary of SiC. The intrinsic defect formation energies are reported in Table 12 and are in good agreement with those from Ref. [39]. The values were calculated using Eq. 3.1 and only the chemical potential of Si and C in Si-rich were

considered for the data in Table 12. The Si and C vacancy defect formation energies in bulk SiC are also listed.

Looking at the intrinsic defect formation energies in the grain boundary, the C vacancies required less energy to form than the vacancies of Si. The similar behavior of lower formation energies in C vacancy is also found for the intrinsic defects in the bulk. Due to the smaller atomic radius of C, it requires less energy to form a C vacancy than a Si vacancy. In addition, because the bi-crystal grain boundary model indicates that grain 1 and grain 2 are asymmetrical with a different orientation of the adjoining crystal and the grain boundary plane (Figure 7), different formation energies for similar defect types from both data sets were obtained.

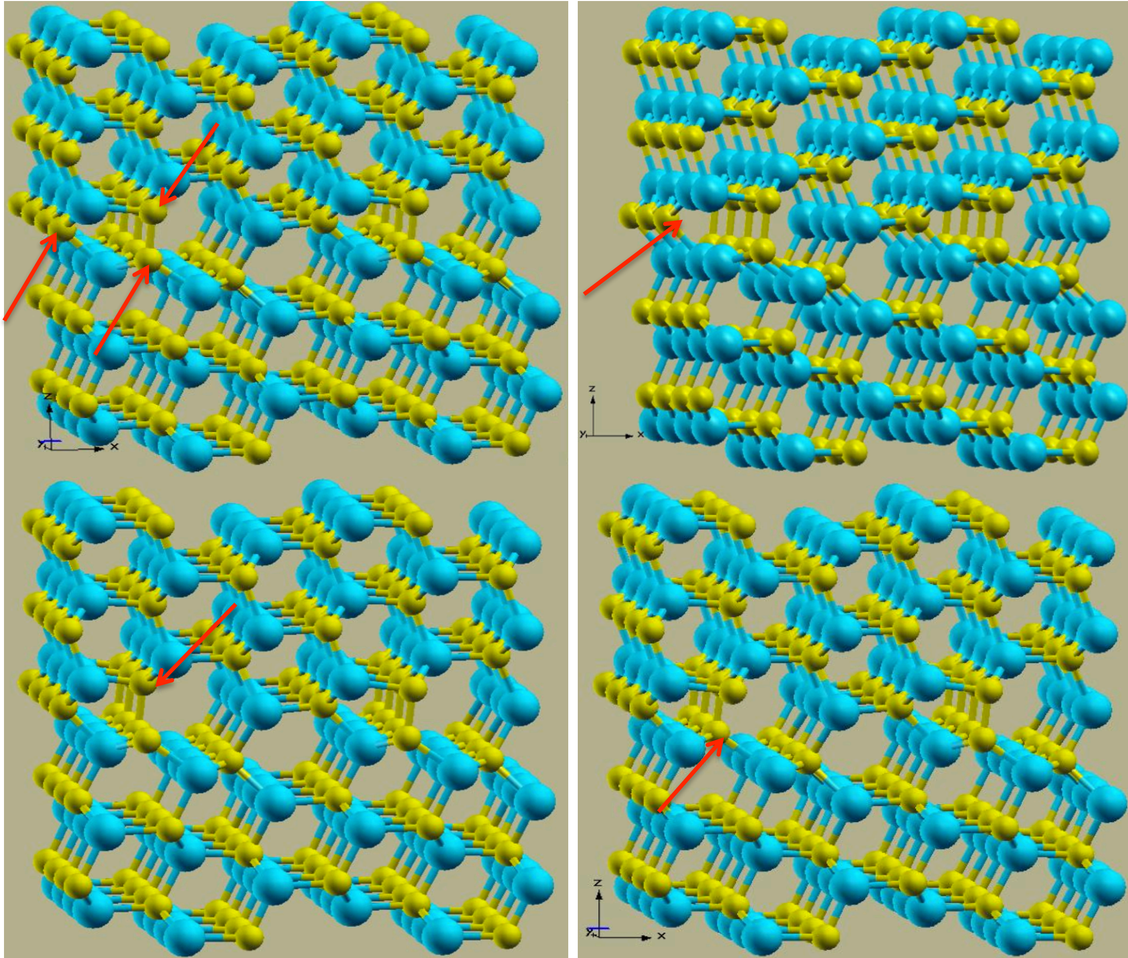

Figure 19 Crystal structure of single C vacancies in GB SiC includes: the complete GB SiC structure with three original C atoms (top left), C vacancy at GB plane (top right), C vacancy at G1 (above the GB plane) (bottom left), and C vacancy at G2 (below the GB plane) (bottom right).

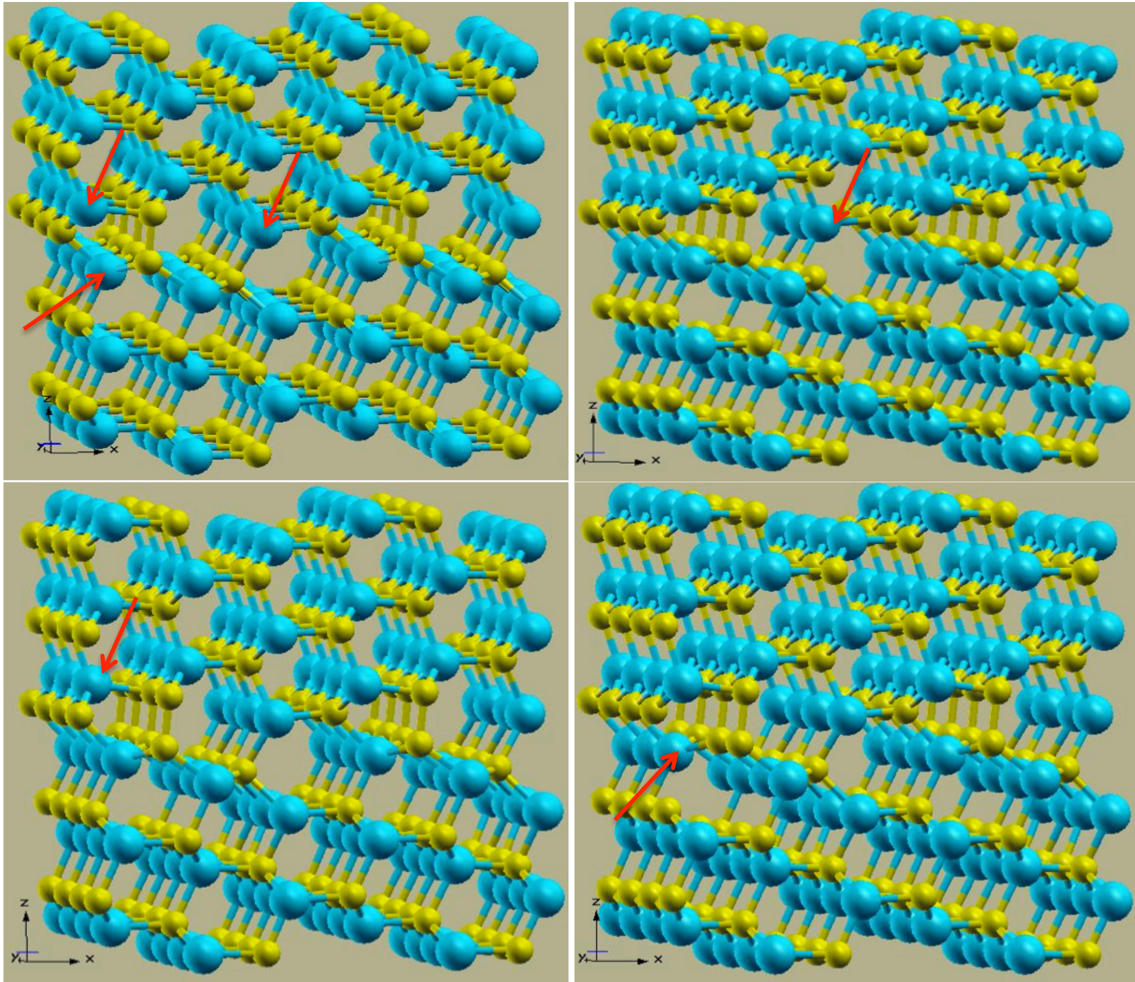

Figure 20 Crystal structure of single Si vacancies in GB SiC includes: the complete structure of GB SiC with three original Si atoms (top left), Si vacancy at GB plane (top right), Si vacancy at G1 (bottom left), and Si vacancy at G2 (bottom right).

Table 12 Results of formation energies for intrinsic defects in the bulk and at the grain boundary of SiC

System	Present work (eV)	[30, 39] (eV)
V_C in bulk SiC	4.38	4.13
V_C in GB plane	3.08	2.78
V_C in grain 1	2.20	1.97
V_C in grain 2	2.18	1.32
V_{Si} in bulk SiC	7.62	7.63
V_{Si} in GB plane	4.89	4.13
V_{Si} in grain 1	5.71	5.81
V_{Si} in grain 2	5.26	4.52

Data from Table 12 indicates that the formation energies of C and Si vacancies in the bulk are higher than that for C and Si vacancies in the grain boundary of SiC. In the crystalline 3C-SiC structure, it is thermodynamically stable when 4 nearest neighbor atoms are surrounding C and Si. Therefore, it will take a large amount of energy to disrupt the lattice to generate a vacancy of C or Si. On the other hand, along the grain boundary of SiC, some C and Si sites are thermodynamically stable with only 3 nearest neighbors. Thus, the formation energies for Si and C vacancies at the grain boundaries are lower than in the bulk SiC because it takes less energy to break the bonds. The high values of vacancy formation energies for C and Si (4.28 eV and 7.62 eV, respectively) prevent substitutional diffusion in the bulk. In Σ3-grain boundary, formation energies of C and Si vacancies are reduced to 2.18 eV and 4.89 eV, respectively. Therefore, Cs will be enriched along the grain boundaries rather than in the bulk of SiC.

4.3.2: Cs Point Defects in the Grain Boundary of SiC

The formation energies of neutral Cs point defects in a Σ3-grain boundary are listed in Table 13. Overall, the lowest formation energy corresponds to Cs substituting Si sites along the grain boundary plane. Due to the large amount of computational time and resources needed, calculations for complex defects of Cs vacancy clusters and charged defects in the grain boundary of SiC were beyond the permitted time frame of this research. The formation energy of neutral Cs substituted defects in bulk SiC (Table 11) is roughly three times more than that of the neutral Cs substituted defects at grain boundary SiC shown in Table 13. In comparison, data from Table 11 indicates that the Cs substituting Si site in association with one C vacancy is the most stable state of Cs in bulk SiC. However, data in Table 13 shows that the Cs substituting Si site along the grain boundary plane is much more energetically favorable even without an additional vacancy. Furthermore, in comparison to the data for Cs defects in bulk SiC, the lower defect formation energies indicate that Cs has higher solubility when it is at the grain boundary. It is known that the grain boundaries provide an easy path for matter transport, leading to a faster diffusion at the grain boundaries than in the bulk [63]. In addition, atoms diffusing along the grain boundary can penetrate deeper into the material than atoms that are only diffusing through the bulk due to a lower migration barrier at grain boundaries [63]. Therefore, with lower defect formation energies, Cs has a strong tendency to segregate to the grain boundaries of SiC.

The formation energies of Ag substitution defects in grain boundary, studied by Khalil *et al.* [39], are also shown in Table 13. According to the data in Table 13, the most stable state for Cs in grain boundary of SiC is Cs substituting Si in the grain boundary

plane. However, the most stable state for Ag in grain boundary of SiC is Ag substituting C in grain 1. On the other hand, both Cs and Ag substituting Si in grain 1 have the highest formation energies.

Table 13 Results for neutral Cs substitution defect formation energies in GB SiC

System	Present work (eV)	System	Khalil *et al.* [39](eV)
Cs_C in GB plane	4.72	**Ag_C in GB plane**	5.60
Cs_C in grain 1	3.70	**Ag_C in grain 1**	3.63
Cs_C in grain 2	5.00	**Ag_C in grain 2**	4.22
Cs_{Si} in GB plane	2.67	**Ag_{Si} in GB plane**	4.01
Cs_{Si} in grain 1	6.76	**Ag_{Si} in grain 1**	6.15
Cs_{Si} in grain 2	5.08	**Ag_{Si} in grain 2**	5.18

In general, both data sets in Table 13 show the lower defect formation energies in the grain boundaries than in the bulk SiC. In the grain boundary of SiC, the values for Cs and Ag defect formation energies are quite close to each other, while they are distinctively different in the bulk (Table 11) with higher formation energies for Cs defects. This is due to the disrupt structure in the grain boundary of SiC, leading to some large spaces around the Si and C atoms. When the substitutions occur, Cs with larger atomic size than Ag would fill in those big gaps and create less strain on its surrounding than Ag. Therefore, some Cs substitution defects even have lower formation energies than Ag defects along the grain boundaries.

In addition, Khalil *et al.* found that Ag diffusion along the grain boundary of SiC is much faster than diffusion in the bulk [39]. However, comparing data for Ag defects between Table 11 and Table 13, the differences in formation energies of some Ag defects

in the bulk and grain boundary of SiC are not significant. It indicates that Ag fission products will be found in the bulk and well as at the grain boundaries of SiC. Whereas, for Cs, the defect formation energies in the bulk and the grain boundaries are very different, indicating that Cs fission products will mostly be found at the grain boundaries than in the bulk SiC.

CHAPTER 5: SUMMARY AND FUTURE WORK

The plane-wave pseudo-potential approach based on density functional theory with the generalized gradient approximation has been used to determine the material properties of pure SiC and to investigate the structural stability of Cs in two different SiC systems, the bulk and the Σ3-grain boundary SiC. Specific observations include the following:

- From the calculations in pure SiC, the equilibrium lattice constant, bulk modulus, and cohesive energy were calculated to be 4.38 Å (8.28 Bohr), 210 MPa, and 7.51 eV/atom, respectively. These baseline calculations for 3C-SiC are in excellent agreement with experimental data (4.36 Å (8.24 Bohr), 225 MPa, and 6.34 eV/atom, respectively, [43]) and theoretical data (227 MPa, 7.55 eV/atom [43]) reported in the literature (Table 4). For pure SiC, the projected wave function calculation of the charge distribution verified, as expected, that the Si-C bond in 3C-SiC has an ionic characteristic with approximately 1.0 electron transferred from Si to C. This also agrees well with previous work (0.98 electrons, [2, 51]). These agreements for pure SiC provided the confidence that the current simulation model was capable of calculating reliable and robust physical and chemical properties of Cs-doped SiC.

- The calculated formation energies of neutral Cs defects in bulk SiC were comparable with the data reported by Shrader *et al.*, where the most probable stable state of neutral Cs in SiC is for Cs to sit at a Si site in association with a C vacancy. The formation energies of neutral Cs defects at the SiC grain boundary were found to be much lower than that in the bulk SiC. This suggests that Cs has a greater solubility at the grain boundary than in the bulk. As a result, Cs diffusion through the SiC layer in TRISO fuel will most likely be found along the grain boundaries.
- Although the defect energies calculated in this investigation suggest that Cs may diffuse through SiC along the grain boundaries, the data only contained results for neutral Cs defects and did not reveal enough information of what the exact diffusion mechanism Cs would take at the grain boundary SiC. Therefore, a further investigation on the charged defects, diffusion coefficients, and the migration barrier (e.g., activation energy) of Cs along the grain boundary is needed to provide a more solid conclusion for how Cs diffuses in SiC.

REFERENCES

1. Agency, I.A.E., *Fuel performance and fission product behavior in gas cooled reactors.* IAEA-TECDOC, 1997. **978**.
2. Snead, L.L., et al., *Handbook of SiC Properties for Fuel Performance Modeling*. 2007. Medium: ED; Size: 329.
3. Shrader, D., I. Szlufarska, and D. Morgan, *Cs diffusion in cubic silicon carbide.* Journal of Nuclear Materials, 2012. **421**(1–3): p. 89-96.
4. Carroll, R.M., R.B. Perez, and O. Sisman, *Release of Fission Gas During Fissioning of UO2.* Journal of the American Ceramic Society, 1965. **48**(2): p. 55-59.
5. Protection, R., *Cesium.* U.S. Environmental Protection Agency, 2012.
6. Todd Allen, J.B., Mitch Meyer, david Petti, *Materials Challenges for Nuclear Systems.* Materialstoday, 2010. **13**.
7. Jürgen Hafner, C.W., Gerbrand Ceder, *Toward Computational Materials Design: The Impact of Density Functional Theory on Materials Research.* MRS Bulletin, 2006. **31**: p. 659-668.
8. Rappoport, F.F.a.D., *Density functional methods for excited states: equilibrium structure and electronic spectra.* Theoretical and Computational Chemistry, 2005. **16**: p. 93-128.
9. Burke, K., *The ABC of DFT*. 2007: Department of Chemistry, University of California, Irvine, CA 92697.
10. Gabor Csanyi, T.A., M. C. Payne, and A. De Vita, *"Learn on the Fly": A Hybrid Classical and Quantum-Mechanical Molecular Dynamics Simulation.* Physical Review Letters, 2004. **93**.
11. Gali, A., *Time-dependent density functional study on the excitation spectrum of point defects in semiconductors.* physica status solidi (b), 2011. **248**(6): p. 1337-1346.
12. David S. Sholl, J.A.S., *Density Functional Theory: A Practical Introduction*. 2009: Wiley. 238.
13. Mattsson, M.T.L.a.A.E., *High-performance computing for materials design to advance energy science.* MRS Bulletin, 2011. **36**: p. pp 169-174.
14. Mattausch, A., *Ab initio-Theory of Point Defects and Defect Complexes in SiC*. 2005.
15. Payne, M.C., et al., *Iterative minimization techniques for ab initio total-energy calculations: molecular dynamics and conjugate gradients.* Reviews of Modern Physics, 1992. **64**(4): p. 1045-1097.
16. Chelikowsky, J.R., *The Pseudopotential-Density Functional Method (PDFM) Applied to Nanostructures.* University of Minesota.
17. C. Jay Smallwood, R.E.L., William J. Glover, Benjamin J. Schwartz, *A computationally efficient exact pseudopotential method. I. Analytic reformulation*

of the Phillips-Kleiman theory. The Journal of Chemical Physics 2006. **125, 074102**.

18. Vanderbilt, D., *Soft self-consistent pseudopotentials in a generalized eigenvalue formalism.* Physical Review B, 1990. **41**(11): p. 7892-7895.
19. Hamann, D.R., M. Schlüter, and C. Chiang, *Norm-Conserving Pseudopotentials.* Physical Review Letters, 1979. **43**(20): p. 1494-1497.
20. John T. Maki, D.A.P., Darrell L. Knudson, Gregory K. Miller, *The challenges associated with high burnup, high temperature and accelerated irradiation for TRISO-coated particle fuel.* Journal of Nuclear Materials, 2007. **271**: p. 270-280.
21. Williams, D., *The Evolution of the Pebble Bed Reactor*, in *Nuclear Power Industry News*. 2009.
22. IAEA, *High Temperature Gas Cooled Reactor Fuels and Materials.* International Atomic Energy Agency, Vienna, Austria, March 2010.
23. Geoffrey Rothwell, J.R., *On the Optimal Lifetime of Nuclear Power Plants.* Journal of Business and Economic Statistic, 1997. **15**: p. 195-208.
24. Gregory K. Miller, D.A.P., John T. Maki, Darrel L. Knudson, *An evaluation of the effects of SiC layer thinning on failure of TRISO-coated fuel particles.* Journal of Nuclear Materials, 2006. **355**: p. 150-162.
25. Meyer Steinberg, J.R.P., *APEX Nucleau Fuel Cycle For Production of LWR Fuel and Elimination of Radioactive Waste.* Brookhaven National Laboratory, 1981.
26. Park, Y.S., *SiC Materials and Devices*. Vol. 52. 2006: Semiconductors and Semimetals.
27. Peiji Zhao, D.W., Jorge M. Seminario, Robert Trew, *Mixed- Valence Transition Metal Complex Based Integral Architecture for Molecular Computing (I): Attachment of Linker Molecule To Silicon (100)-2x1 Surface.* International Journal of High Speed Electronics and Systems, 2006. **16**: p. 705-712.
28. Roma, G., *Palladium in cubic silicon carbide: Stability and kinetics.* Journal of Applied Physics, 2009. **106**(12): p. 123504-9.
29. Van Ginhoven, R.M., et al., *Theoretical study of helium insertion and diffusion in 3C-SiC.* Journal of Nuclear Materials, 2006. **348**(1–2): p. 51-59.
30. Shrader, D., et al., *Ag diffusion in cubic silicon carbide.* Journal of Nuclear Materials, 2011. **408**(3): p. 257-271.
31. López-Honorato, E., et al., *TRISO coated fuel particles with enhanced SiC properties.* Journal of Nuclear Materials, 2009. **392**(2): p. 219-224.
32. Amian, W. and D. Stover, *Diffusion of silver and cesium in silicon-carbide coatings of fuel particles for high-temperature gas-cooled reactors.* Journal Name: Nucl. Technol.; (United States); Journal Volume: 61:3, 1983: p. 475-486.
33. E. Friedland, J.B.M., N.G. van der Berg, T. Hlatshwayo, A.J. Botha, E. Wendler, W. Wesch, *Study of silver diffusion in silicon carbide.* Journal of Nuclear Materials, 2009. **389**: p. 326-331.
34. MacLean, H.J., *Silver Transport in CVD Silicon Carbide.* PhD Thesis, Department of Nuclear Engineer, MIT, Boston, 2004.
35. Allelein, H.J., *Kernforschungsanlage Julich GmbH.* Institut Fur Reajtorentwicklung, Jul, 1980(1695).
36. Kazuo Minato, T.O., Kousaku Fukuda, Hajime Sekino, Hideyuki Miyanishi, Shigeo Kado, Ishio Takahashi, *Release behavior of metallic fission products from*

HTGR fuel particles at 1600 to 1900°C. Journal of Nuclear Materials, 1993. **202**(1-2): p. 47-53.

37. Nabielek, H., P.E. Brown, and P. Offermann, *Silver release from coated particle fuel.* Journal Name: Nucl. Technol.; (United States); Journal Volume: 35:2, 1977: p. Medium: X; Size: Pages: 483-493.
38. Karl Verfondern, R.C.M., Rainer Moormann, *Methods and data for HTGR fuel performance and radionuclide release modeling during normal operation and accidents for safety analyses*. 1993: Forschungszentrum Juelich G.m.b.H. (Germany, F.R.).
39. Khalil, S., et al., *Diffusion of Ag along Σ3 grain boundaries in 3C-SiC.* Physical Review B, 2011. **84**(21): p. 214104.
40. Quantum-ESPRESSO, *http://www.quantum-espresso.org/.*
41. Pseudopotentials, *http://www.quantum-espresso.org/?page_id=190.*
42. Priya Vashishta, R.K.K., Aiichiro Nakano, Jose Pedro Rino, *Interaction potential for silicon carbide: A molecular dynamics study of elastic constants and vibrational density of states for crystalline and amorphous silicon carbide.* Journal of Applied Physics, 2007. **101**(103515).
43. Feng, Z.C., *SiC Power Materials: Devices and Applications*. 2004: Springer.
44. Chris G. Van de Walle, J.N., *First-principles calculations for defects and impurities: Applications to III-nitrides.* Journal of Applied Physics Reviews, 2004. **95**.
45. M Posselt, F.G., W J Weber, and V Belko, *A comparative study of the structure and energetics of elementary defects in 3C- and 4H-SiC* Journal of Physics: Condens. Matter 2004. **16**: p. 1307-1323.
46. Paolo Giannozzi (Input-pw.txt), *Input file description for calculation in Quantum-espresso.*
47. Cheng-Zhang Wang, R.Y., and Henry Krakauer, *Pressure dependence of Born effective charges, dielectric constant, and lattice dynamics in SiC.* Physical Review B, 1996. **53**(Number 9).
48. Fei Gao, E.J.B., William J. Weber, L. Rene Corrales, *Native defect properties in β-SiC: Ab initio and empirical potential calculations.* Nuclear Instruments and Methods in Physics Research Section B, 2001. **180**(1-4): p. 286-292.
49. Ziambaras, E. and E. Schröder, *Theory for structure and bulk modulus determination.* Physical Review B, 2003. **68**(6): p. 064112.
50. K. Karch, P.P., W. Windl, D. Strauch, F. Bechstedt, *Ab Initio Calculation of Structural, Lattice Dynamical, and Thermal Properties of Cubic Silicon Carbide.* International Journal of Quantum Chemistry, 1995. **56**: p. 801-817.
51. David Ayma, M.R., Roberto Orlando, and Albert Lichanot, *Ab Initio Calculation of the Structure Factors and Compton Profiles of Cubic Silicon Carbide.* Acta Crystallographica Section A, 1998. **54**: p. 1019-1027.
52. Liu Hong-Sheng, F.X.-Y., Song Wei-Li, Hou Zhi-Ling, Lu Ran, Yuan Jie, Cao Mao-Sheng, *Modification of Band Gap of β-SiC by N-Doping* Chin. Phys. Lett, 2009. **26**(No. 6).
53. G L Zhao, D.B., *Electronic structure and charge transfer in 3C- and 4H-SiC.* New Journal of Physics, 2000. **2**(16): p. 1-16.

54. Dou Yan-Kun, Q.X., Jin Hai-Bo, Cao Mao-Sheng, Usman Zahid, Hou Zhi-Ling, *First Principle Study of the Electronic Properties of 3C-SiC Doped with Different Amounts of Ni.* Chin. Phys. Lett, 2012. **29**(No. 7).
55. Santos de Oliveira, I.S. and R.H. Miwa, *Boron and nitrogen impurities in SiC nanowires.* Physical Review B, 2009. **79**(8): p. 085427.
56. Zunger, S.L.a.A., *Assessment of correction methods for the band-gap problem and for finite-size effects in supercell defect calculations: Case studies for ZnO and GaAs.* Physical Review B, 2008. **78**.
57. Murdock, D., *Worked Exampleds from Introductory Physics (Algebra-Based), Vol. IV: Electricity*. January 20, 2008.
58. Gatti, C., *Modern Charge-Density Analysis*, ed. P. Macchi. 2012: Springer.
59. Binghai Yan, C.P., Jisoon Ihm, Gang Zhou, Wenhui Duan, Noejung Park, *Electron Emission Originated from Free-Electron-like States of Alkali-Doped Boron#Nitride Nanotubes.* Journal of the American Chemistry Society, 2008. **130**(50): p. 17012-17015.
60. Glötzel, D. and A.K. McMahan, *Relativistic effects, phonons, and the isostructural transition in cesium.* Physical Review B, 1979. **20**(8): p. 3210-3216.
61. G. Lucas, L.P., *Structure and stability of irradiation-induced Frenkel pairs in 3C-SiC using first principles calculations.* Nuclear Instruments and Methods in Physics Research Section B, 2007. **255**(124-129).
62. Takashi Sawabe, M.A., Katsumi Yoshida, Toyohiko Yaho, *Estimation of neutron-irradiation-induced defect in 3C-SiC from change in XRD peak shift and DFT study.* Journal of Nuclear Materials, 2011.
63. David A. Porter, K.E.E., and Mohamed Y. Sherif, *Phase Transformations in Metals and Alloys*. Vol. 3rd ed. 2009: CRC Press, Taylor and Francis Group.